Constraints on planetary formation, accretion and differentiation from experimental petrology

Steenstra, E.S.

2019

document version
Publisher's PDF, also known as Version of record

Chapter 11

The effect of temperature on the metal-silicate partitioning of volatile siderophile elements: implications for volatile element depletions in the Moon and Mars

This chapter is in preparation for publication as: *Steenstra E.S., Berndt J., Klemme S., van Westrenen W., Fei Y. The effect of temperature on the metal-silicate partitioning of volatile siderophile elements: implications for volatile element depletions in the Moon and Mars.*

ABSTRACT

The abundances of volatile siderophile elements (VSE) in planetary mantles are determined by a range of volatile depletion processes during accretion, core formation, magma ocean crystallization and secondary volcanism. Assessment of the relative importance of these processes in the Moon and Mars requires a quantitative understanding of the variability of VSE metal-silicate partition coefficients (D's). We studied the effects of temperature on VSE D's by performing high-pressure equilibration experiments at pressures between 3 and 6 GPa and temperatures between 1973 and 2873 K. Results indicate that at constant pressure $D^{met-sil}_{S,\ Ge,\ Se,\ Sn,\ Te}$ decrease with increasing temperature. Temperature has negligible effects on the partitioning behavior of Cu, In and Sn, whereas $D^{met-sil}_{Ga,\ Cd,\ Pb}$ values increase with increasing temperature. Temperature appears to decrease the siderophile behavior of As, Mo, Sb and increase $D^{met-sil}_{P,\ W}$, but silicate melt compositional effects rather than temperature itself may cause these trends. Previously proposed positive pressure dependencies of log $D^{met-sil}_{S,\ Se,\ Te}$ are reproduced within error. Except for Cu, D values do not vary with pressure in the 3 to 6 GPa range.

Application of our results to the Moon confirms previous hypotheses related to the importance of core formation on the volatile element budget of the lunar mantle. The depletions for some volatile elements (Zn, Ga, Cd, In, Pb) cannot be explained solely by core formation, suggesting additional loss of these elements occurred through volatility-related processes during the Moon-forming event and/or subsequent magma ocean differentiation. In contrast, depending on the effects of pressure, VSE depletions in the Martian mantle are likely to be largely if not fully explained by formation of a S-rich Martian core.

11.1 INTRODUCTION

Core formation in both the Moon and Mars likely occurred in a magma ocean-type setting (e.g. Wood et al., 1970; Debaille et al., 2007). The Moon is believed to have formed through a highly energetic giant impact event, which could have resulted in very high temperatures during its formation and initial differentiation (Thompson and Stevenson, 1988; Canup, 2004; Pahlevan and Stevenson, 2007; Salmon and Canup, 2012; Steenstra et al., 2016a; Lock et al., 2018; Chapter 16). Current estimates of the temperatures in the Moon-forming disk following the giant impact from the latter studies range between 2000 and 7000 K. The siderophile element geochemistry of the lunar mantle may record the final moment of metal-silicate equilibrium in a fully molten Moon following rigorous convection, as implied from its anomalous Ni/Co ratio and net abundances of Cr, Co and Ni (see Chapter 16). For Mars, the existence of large-scale Martian magma ocean is implied from its very early differentiation age (<20 Myr) derived from geochemical analyses of SNC meteorites (Dauphas and Pourmand, 2011; Tang and Dauphas, 2014; Bouvier et al., 2018). Bouvier et al. (2018) recently reported zircon U/Pb ages of a Martian regolith breccia that suggests accretion, core formation and magma ocean crystallization on Mars was completed within 20 Myr after the formation of the solar system. This is consistent with the differentiation ages of <2.5 Myr obtained from Hf-W-Th systematics (Dauphas and Pourmand, 2011). Such early timing of Martian differentiation implies that many short-lived heat-producing radio-isotopic systems were still live. This heat source, combined with gravitational and impact heating, should have been sufficient for large-scale melting of Mars. Core formation in Mars may have occurred at temperatures close to or higher than the Martian mantle liquidus at the core/mantle boundary (estimated at ~2500 K; Righter and Chabot, 2011).

We and other workers have shown in several recent studies that planetary cores, including those of the Moon and Mars, can be significant reservoirs for various volatile elements including S, Se, Te, Sb, Sn and Cu (e.g. Yang et al., 2015; Righter et al., 2018a; Steenstra et al., 2016a; 2017c; 2018). To assess to which extent such models are sensitive to the very high temperatures that may have been associated with core formation in Moon and Mars, the effects of temperature on the metal-silicate partitioning of volatile siderophile elements needs to be constrained. In previous studies, such effects were mainly determined via multi-linear regression of datasets obtained at lower temperatures than those relevant for the recently proposed higher-temperature core formation scenarios in Mars and the Moon discussed above. We have undertaken an experimental study to quantify the effects of temperature on volatile siderophile element partitioning for both S-free and S-rich alloys, relevant for the Moon and Mars, respectively.

11.2 METHODS

11.2.1 High pressure-temperature experiments

To assess the effects of temperature on the metal-silicate partitioning of volatile siderophile elements, we performed high-pressure metal-silicate partitioning experiments in a 1500-ton multi-anvil apparatus at the Geophysical Laboratory, Carnegie Institution for Science, at temperatures of up to 2873 K (Table 11.1). Experiments were conducted using 18mm edge length Cr-doped MgO or ZrO_2 octahedra, graphite heaters and polycrystalline 1.6 mm I.D. MgO capsules. Pressure calibration was based on the qtz-coes and gt-pv transitions, resulting in an estimated pressure uncertainty of ~0.2 GPa (Corgne et al., 2007). Experiments were performed using a synthetic analogue powder of a primitive lunar basalt (Apollo 15 green glass, Delano, 1986a). Three types of synthetic metal powder mixtures were used. The first mixture (A) consisted of Fe powder with 1 wt.% Si, 5 wt.% Ni and 1.5 wt.% of As, Se, Cd, In, Sb, Te and Pb. The second mixture (B) was prepared by doping Fe powder with 10 wt.% S, added through addition of the appropiate amounts of FeS and 1.5 wt.% of Mn, Cu, Zn, Nb, Cd, In, Sn, Ta. The third mixture (C) was obtained by adding 5 wt.% S through addition of FeS to mixture A. All of the chemical powders used were of high purity (>99.8%, except Fe with >99.5%, Alfa Aesar). Powders were loaded into the MgO capsules in a silicate-metal volume ratio of ~2:1.

Before heating, samples were pressurized to target pressures. Temperature was monitored and controlled using a Type C (95%W/5%Re - 74%W/26%Re) thermocouple placed directly above the sample container at the assembly hotspot. Experimental charges were then heated at 100 K per minute to 1273 K, after which they were sintered for 60 to 120 min to reduce porosity of the MgO capsule. After sintering samples were heated to target temperature at a rate of 100 K/min. For target temperatures exceeding 2473 K, experimental temperatures were estimated using well-defined power-temperature relationships (Chapter 16) due to the melting of thermocouple wires. Uncertainties on estimated temperatures are ±50 K. Metals and silicates were equilibrated at peak temperatures between 10 and 0.5 min, depending on final temperature. As discussed in other chapters, such run times have been shown to be sufficient for attainment of metal-silicate equilibrium in comparable experimental set-ups (e.g. Thibault and Walter, 1995; Wade and Wood, 2005; Siebert et al., 2011; Tuff et al., 2011). Experiments were rapidly quenched by shutting off the power to the furnace and recovered samples were mounted in petropoxy resin. Samples were then polished using various grades of Al polishing powder and carbon coated for subsequent chemical analyses with EPMA and LA-ICP-MS techniques.

Table 11.1 *Experimental run conditions, starting materials and details related to fO_2 conditions*

Run #	*P* (GPa)	*T* (K)	Time (s)	Comp.[b]	γ_{Fe}^{metal}	ΔIW [c]
PR1490	3.8	1973	600	GG + A	0.99	–2.74
PR1509	4.9	2473	120	GG + A	1.00	–2.42
PR1519[a]	4.4	2473	120	GG + A	1.00	–2.67
PR1520	2.7	2473	120	GG + A	1.00	–3.45
PR1523	5.8	2473	120	GG + A	1.00	–2.49
PR1540	5.4	2473	120	GG + A	1.00	–2.48
PR1556	5.2	2273	20	GG + A	1.00	–1.76
PR1466	4.7	2273	180	GG + B	1.32	–1.64
PR1467	3.8	2073	180	GG + C	1.19	–1.62
PR1471	4.9	2273	180	GG + B	1.16	–1.76
PR1478	3.8	2373	90	GG + C	1.19	–2.15
PR1479	3.8	2273	90	GG + C	1.16	–1.81
PR1482	3.8	2550[d]	40	GG + C	1.14	–1.96
PR1486	3.8	2173	180	GG + C	1.13	–1.58
PR1487	3.8	2073	240	GG + D	1.00	–2.00
PR1488	3.8	1973	360	GG + C	1.09	–1.77
PR1503	3.8	2573[d]	60	GG + C	1.11	–1.99
PR1504	3.8	2673[d]	30	GG + C	1.13	–1.98
PR1529	3.8	2773[d]	30	GG + C	1.11	–1.83
PR1530	3.8	2873[d]	20	GG + C	1.09	–1.78
PR1531	3.8	2873[d]	30	GG + C	1.13	–1.72
PR1537	2.7	2473	120	GG + C	1.05	–1.99
PR1548	3.8	2473	90	GG + C	1.14	–1.81
PR1549	4.9	2573[d]	80	GG + C	1.13	–1.88
PR1551	3.8	1973	180	GG + C	1.18	–1.17
PR1557	5.2	2263[d]	180	GG + C	1.18	–1.52

[a] Low total of the metal phase in this experiment suggests significant contamination of C from the graphite heater and was therefore excluded from subsequent calculations [b] GG = lunar Apollo 15 green glass; A-C denote the type of metal composition used in the experiments (A = Fe + 1 wt.% Si, 5 wt.% Ni, 1.5 wt.% As, Se, Cd, In, Sb, Te, Pb; B = Fe + 10 wt.% S, 5 wt.% Ni, 1.5 wt.% As, Se, Cd, In, Sb, Te, Pb; C = Fe + 10 wt.% S, 1.5 wt.% Mn, Cu, Zn, Nb, Cd, In, Ta [c] Calculated assuming γ_{FeO}^{sil} = 1.7 [d] Temperature was estimated using power-*T* relationships derived from thermocouple measurements up to ~2500 K from multiple experiments at the same pressures and with the same assembly; uncertainties are ±50 (see Chapter 16).

11.2.2 Analytical methods

Metals and silicates were analyzed for major element abundances using a JEOL JXA-8530F electron probe microanalyser at the University of Münster, Germany (Tables 11.2, 11.3). Both sulfides and silicates were analyzed with a defocused 15 µm diameter beam. The EPMA analyses were conducted using beam currents of 20 nA and an accelerating voltage of 15 kV. Counting times were 30 s for peak and 15 s for background for major elements (Si, Al, Ti, Cr, Mg, Fe, Mn, Ca), whereas counting times of 20 s peak and 10 s background were used for S. Measurement points were set in lines and/or raster grids, depending of the available surface area of the analysed phases, with step sizes approximately equivalent to the beam size. Metal standards were $KTiPO_5$ for P, TiO_2 for Ti, tephroite for Mn, galena for Pb, InAs for In and As, CdS for Cd, diopside for Si, chalcopyrite for S, and pure metal standards for V, Cr, Fe, Co, Ni, Cu, Zn, Ge, Se, Sn, Sb, Te, Mo, and W. Silicate analyses were calibrated using diopside for Si and Ca, forsterite for Mg, corundum for Al, hematite for Fe, tephroite for Mn, galena for Pb, InAs for In and As, CdS for Cd, $KTiPO_5$ for P and K, TiO_2 for Ti, jadeite for Na and pure metal standards for V, Cr, Fe, Ni, Cu, Zn, Ge, Se, Sn, Sb, Te, Mo, and W. Calibrations were considered successful when the primary standard compositions were reproduced within 1%

relative deviation. Data reduction was performed using the Φ(ρZ) correction (Armstrong, 1995). For additional details on EPMA analyses, including information about the calibration of silicate phases, the reader is referred to Steenstra et al. (2017b,c).

Laser ablation inductively coupled plasma mass spectrometry (LA-ICP-MS) at the University of Münster was used to quantify the abundances of trace elements in the metal and silicate melts (Tables 11.2, 11.3). These analyses were performed using a 193 nm ArF excimer laser (Analyte G2, Photon Machines) with a repetition rate of 10 Hz and energy of ~3–4 J/cm^2 throughout the entire analytical session with beam sizes ranging between 25–50 µm. The following isotopes were measured: ^{29}Si, ^{31}P, ^{43}Ca, ^{49}Ti, ^{48}Ti, ^{51}V, ^{53}Cr, ^{55}Mn, ^{59}Co, ^{60}Ni, ^{61}Ni, ^{63}Cu, ^{66}Zn, ^{69}Ga, ^{73}Ge, ^{75}As, ^{82}Se, ^{93}Nb, ^{95}Mo, ^{118}Sn, ^{121}Sb, ^{125}Te, ^{181}Ta, ^{182}W and ^{208}Pb. The NIST 612 glass was used as an external reference material for both the metal and silicate. Concentrations of Si in the silicate melt and Ni or Cu concentrations of the metallic melts were used as internal standards. Copper was chosen as an internal standard for S-rich experiments as no non-volatile, non-refractory elements were present in sufficient quantities in the metal to be used as an internal standard. Copper is very homogeneously distributed in the metal phase and is present in significant quantities in the NIST 612 glass and other reference materials (Chapter 2; Table 11.3). We have shown in Chapter 2 that Cu is fractionated due to the use of non-matrix-matched silicate primary standards. To address this issue, we corrected measured EPMA concentrations of Cu using the empirical correction term from Chapter 2 and used these values as internal standards for LA-ICP-MS data processing.

USGS reference materials BIR-1G and BCR-2G were analyzed every ~20 LA-ICP-MS spots to assess the analytical accuracy and precision of measured trace element concentrations. As discussed in Chapter 2, the use of non-matrix-matched primary standards requires corrections on the LA-ICP-MS measured concentrations of volatile elements in metals. Where necessary, volatile element abundances in metals were therefore corrected using the empirical correction factors reported in Chapter 2. Note that for most volatile elements metal-silicate partition coefficients were largely (Cu, Cd, In, Sn) if not completely (S, P, Ge, As, Se, Sb, Te) based on EPMA metal measurements, so that corrections were not involved in calculation of their D values.

11.3 RESULTS

11.3.1 Run products

Backscattered electron images of typical experimental run products are shown in Fig. 11.1. The silicate melts quenched to a combination of quench crystals and interstitial glass, independent

of run temperatures. Silicate melts in the centers of the samples were typically devoid of ''nuggets''. In some of the more Nb/Ta rich experiments, Nb-Ta-S bearing phases exsolved during quenching (Fig. 11.1). These did not contain significant quantities of other trace elements, so that ''clean'' trace element signals of the silicate melts could be obtained by LA-ICP-MS. The use of MgO capsules resulted in substantial enrichment of silicate melts in MgO. This also resulted in crystallization of ferropericlase crystals in higher-temperature experiments (Fig. 11.1). The metal phases are characterized by their heterogeneous nature. In the case of S-bearing experiments, the Fe-S alloy quenched to S-rich and S-poor phases (Fig. 11.1). In S-free alloys, trace elements exsolved upon quenching, resulting in the formation of phases rich in Se, Cd, Te and Pb (as previously observed in lower temperature experiments, e.g. Rose-Weston et al., 2009; Chapter 6).

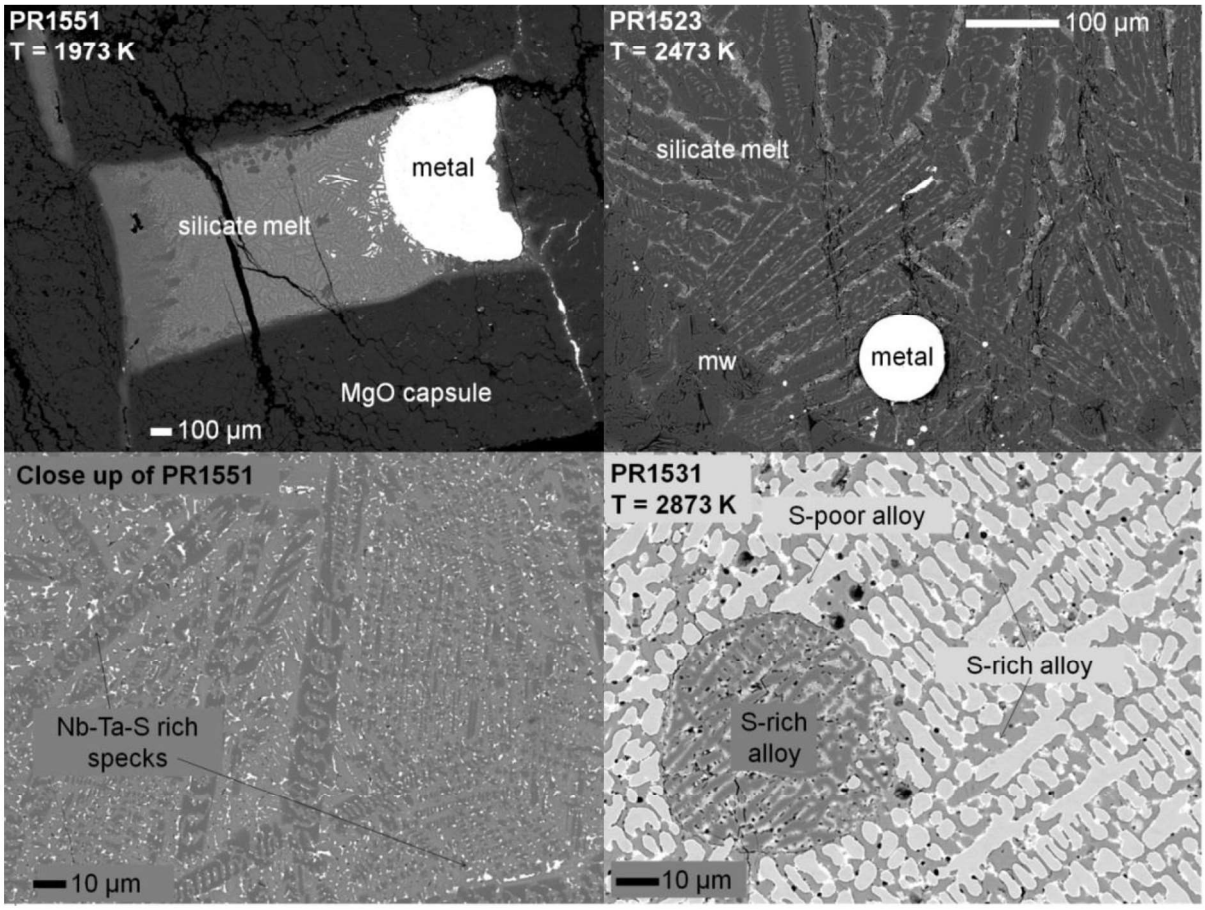

Fig. 11.1 *Backscattered electron images of typical experimental run products.*

Table 11.2 *Composition of silicate melts as determined by EPMA and LA-ICP-MS.*

Run #	**PR1490**	**PR1509**	**PR1519**	**PR1520**	**PR1523**	**PR1540**	**PR1556**	**PR1466**	**PR1467**	**PR1471**	**PR1478**	**PR1479**	**PR1482**	**PR1486**
EPMA	*N = 39* [a]	*N = 14*	*N = 36*	*N = 33*	*N = 53*	*N = 33*	*N = 30*	*N = 29*	*N = 30*	*N = 44*	*N = 30*	*N = 33*	*N = 28*	*N = 32*
MgO (wt.%)	28.05(43)[b]	47.58(143)	48.07(152)	48.30(196)	47.20(163)	46.20(154)	38.11(243)	41.55(317)	36.08(240)	41.00(215)	47.22(183)	42.87(222)	53.2(258)	39.11(243)
SiO_2	49.67(21)	37.50(62)	37.22(80)	38.08(83)	38.31(62)	37.77(66)	36.94(48)	36.24(130)	32.52(121)	36.95(63)	36.21(133)	33.60(131)	21.93(214)	33.25(138)
Al_2O_3	8.26(12)	4.89(83)	5.15(100)	4.78(136)	4.11(73)	5.25(100)	6.67(89)	5.01(139)	5.38(119)	4.24(85)	4.08(155)	4.53(114)	13.44(96)	7.25(166)
CaO	9.89(13)	5.90(73)	5.32(106)	6.58(150)	5.14(113)	5.78(111)	7.58(125)	5.35(169)	6.07(100)	6.47(111)	4.44(109)	5.92(109)	2.64(69)	5.97(113)
FeO	2.97(6)	4.72(26)	3.65(34)	1.47(18)	4.54(38)	4.32(33)	9.27(69)	10.78(143)	10.54(70)	9.06(60)	6.05(69)	8.83(68)	7.48(83)	11.26(115)
K_2O	0.021(2)	n.d.	0.005(3)	0.009(4)	0.009(2)	0.009(3)	0.010(4)	0.008(3)	0.03(1)	0.02(1)	0.009(3)	0.013(4)	b.d.l.	0.07(4)
Na_2O	0.29(1)	n.d.	0.012(5)	0.03(1)	0.008(3)	0.02(1)	0.02(1)	0.01(1)	1.06(24)	0.60(15)	0.07(2)	0.18(4)	0.008(3)	0.19(12)
MnO	0.26(1)	0.10(3)	0.10(2)	0.09(1)	0.12(1)	0.10(1)	0.18(2)	0.11(2)	1.67(13)	0.09(1)	0.61(7)	0.89(8)	0.40(3)	1.46(14)
Cr_2O_3	0.222(4)	0.15(3)	0.14(3)	0.05(2)	0.12(2)	0.13(2)	0.37(4)	0.17(4)	0.14(3)	0.09(1)	0.11(4)	0.14(3)	0.21(13)	0.23(4)
CdO	0.11(1)	b.d.l.	0.03(2)	0.02(1)	0.09(2)	0.12(3)	0.28(4)	0.07(2)	0.11(3)	0.10(2)	0.04(2)	0.08(3)	0.03(1)	0.10(4)
TiO_2	0.25(1)	0.16(3)	0.15(3)	0.15(3)	0.14(3)	0.13(3)	0.24(5)	0.13(5)	0.14(3)	0.15(3)	0.10(4)	0.13(3)	0.08(1)	0.12(2)
In_2O_3	0.07(1)	0.10(1)	0.05(1)	0.02(1)	0.03(1)	0.05(1)	0.10(2)	0.04(2)	0.09(3)	0.06(1)	0.05(2)	0.08(2)	0.02(1)	0.10(3)
SeO_2	b.d.l.[c]	0.14(2)	0.04(2)	0.10(6)	0.02(1)	0.06(3)	0.02(1)	n.d.	–	n.d.	–	–	–	–
TeO_2	b.d.l.	b.d.l.	b.d.l.	0.01(1)	b.d.l.	0.01(1)	b.d.l.	n.d.	–	n.d.	–	–	–	–
SO_3	0.13(6)	b.d.l.	0.02(1)	0.011(5)	0.013(5)	0.01(1)	0.02(1)	0.65(26)	0.99(24)	0.40(10)	0.39(15)	0.72(24)	1.32(22)	0.56(17)
PbO	0.07(1)	0.04(2)	0.03(1)	0.02(1)	0.02(1)	0.05(2)	0.08(2)	n.d.	–	n.d.	–	–	–	–
ZnO	–	–	–	–	–	–	–	–	1.60(32)	–	0.39(6)	0.54(5)	0.38(4)	0.89(18)
CuO	–	–	–	–	–	–	–	–	0.017(5)	–	0.02(1)	0.03(1)	0.02(1)	0.02(1)
Nb_2O_5	–	–	–	–	–	–	–	–	2.56(124)	–	0.63(31)	1.04(33)	0.15(6)	1.38(57)
Ta_2O_5	–	–	–	–	–	–	–	–	2.05(112)	–	0.48(29)	0.73(28)	0.10(8)	0.94(45)
SnO_2	–	–	–	–	–	–	–	–	0.03(2)	–	0.01(1)	0.008(5)	0.01(1)	0.01(1)
ZrO_2	n.d.[d]	n.d.	0.37(9)	0.03(1)	0.06(2)	0.04(1)	0.04(2)	0.10(4)	0.40(8)	0.68(16)	0.06(2)	0.05(1)	0.12(4)	0.02(2)
Sum	100.20(11)	101.30(27)	99.96(42)	99.77(40)	99.85(52)	100.04(27)	99.95(24)	100.30(42)	101.48(117)	99.97(32)	100.99(62)	100.37(43)	101.60(72)	100.65(63)
LA	*N = 9*	*N = 8*	*N = 14*	*N = 7*	*N = 12*	*N = 7*	*N = 12*	*N = 10*	*N = 13*	*N = 9*	*N = 5*	*N = 8*	*N = 7*	*N = 14*
CaO (wt%)	9.51(7)	5.56(43)	4.77(46)	5.22(49)	5.02(55)	5.92(33)	6.78(34)	6.33(58)	5.75(57)	7.04(56)	4.22(149)	5.54(118)	2.78(50)	5.53(44)
Ti (ppm)	1574(11)	875(59)	791(64)	719(102)	843(82)	841(51)	1267(73)	996(82)	965(93)	1069(94)	597(200)	767(112)	506(63)	880(80)
Cr	1533(43)	746(65)	756(34)	335(46)	877(62)	736(66)	2257(83)	992(45)	896(71)	615(64)	799(197)	834(160)	922(210)	1141(63)
Mn	2031(11)	776(19)	836(36)	668(68)	917(58)	811(40)	1302(41)	910(51)	12155(682)	678(22)	4894(626)	6676(791)	3511(478)	10098(477)
Ni	3.8(6)	52(7)	64(4)	9.5(14)	79(8)	59(6)	81(2)	139(12)	–.	67(5)	–	–	–	–
Cu	3.5(6)	1.25(28)	1.71(23)	b.d.l.	1.41(23)	3.1(9)	1.36(7)	5.6(9)	191(16)	7.9(26)	190(61)	229(67)	93(14)	206(17)
Zn	121(3)	11(1)	10(1)	5.3(21)	12(1)	17(2)	23(2)	27(2)	14986(841)	19(1)	4724(760)	5784(551)	4230(911)	6631(345)
Ga	2.23(7)	0.72(10)	0.66(5)	1.00(29)	0.57(6)	0.62(8)	0.96(7)	1.94(15)	1.53(14)	1.78(13)	0.97(43)	2.00(46)	2.21(59)	1.23(10)
As	1.9(4)	1.07(41)	b.d.l.	4.0(20)	b.d.l.	1.2(3)	1.16(37)	1.20(7)	–	b.d.l.	–	–	–	–
Se	104(6)	830(82)	306(28)	961(227)	341(39)	650(21)	270(18)	122(14)	–	162(13)	–	–	–	–
Zr	484(16)	397(40)	2069(194)	202(34)	350(43)	238(18)	38(3)	872(86)	3928(831)	4745(527)	293(110)	241(52)	677(123)	48(4)
Nb	–	–	–	–	–	–	–	–	15456(1757)	–	4101(1584)	7102(1182)	1154(219)	10110(1035)
Cd	1381(194)	1131(97)	585(46)	206(73)	1088(93)	1324(76)	2696(127)	716(84)	1312(135)	953(73)	700(187)	769(158)	292(35)	1165(79)
In	606(21)	514(56)	266(19)	577(204)	391(51)	386(20)	724(32)	524(45)	900(76)	656(44)	632(181)	899(140)	280(51)	668(42)
Sn	0.61(9)	0.18(7)	0.26(4)	0.55(22)	0.26(6)	0.44(14)	<0.11	0.37(6)	132(7)	0.39(8)	50(10)	104(13)	33(11)	99(6)
Sb	1.78(49)	2.4(7)	3.0(4)	1.76(43)	2.0(3)	1.67(36)	2.2(2)	7.1(12)	–	4.0(10)	–	–	–	–
Te	13(3)	158(9)	79(8)	241(88)	86(12)	99(9)	44(2)	28(4)	–	26(3)	–	–	–	–
Ta	–	–	–	–	–	–	–	–	12170(1330)	–	3872(1396)	5688(850)	1221(234)	8623(960)
Pb	863(62)	396(37)	239(20)	84(34)	350(38)	490(79)	739(32)	177(19)	0.81(18)	377(35)	0.46(17)	0.70(12)	0.24(3)	0.15(3)

Run #	**PR1487**	**PR1488**	**PR1503**	**PR1504**	**PR1529**	**PR1530**	**PR1531**	**PR1537**	**PR1548**	**PR1549**	**PR1551**	**PR1557**	**PR1560**
EPMA	*N = 27*	*N = 28*	*N = 24*	*N = 14*	*N = 29*	*N = 29*	*N = 55*	*N = 26*	*N = 31*	*N = 30*	*N = 32*	*N = 32*	*N = 29*
MgO (wt%)	38.69(305)	39.86(131)	49.54(234)	52.48(252)	55.36(178)	54.83(176)	49.02(144)	45.55(188)	48.19(355)	43.34(177)	21.79(183)	35.93(262)	37.70(220)
SiO_2	36.25(113)	34.11(84)	30.86(180)	28.03(228)	25.83(175)	36.33(168)	30.14(116)	34.32(109)	28.75(222)	35.13(117)	39.80(29)	34.07(100)	37.53(69)
Al_2O_3	4.28(103)	6.53(141)	3.74(72)	3.81(91)	3.77(49)	3.11(62)	3.96(61)	4.42(86)	4.80(97)	5.23(108)	7.43(62)	7.02(127)	6.06(74)
CaO	4.81(147)	6.57(68)	4.76(93)	4.11(118)	3.99(61)	3.94(80)	4.55(84)	5.34(102)	6.10(120)	6.15(111)	7.82(72)	7.36(120)	7.74(134)
FeO	7.60(98)	9.30(41)	8.20(75)	7.52(61)	8.92(57)	9.44(64)	9.72(61)	7.53(49)	8.79(81)	8.14(69)	16.30(19)	11.81(96)	9.94(61)

K_2O	0.011(3)	0.02(1)	n.d.	n.d.	0.007(3)	0.009(4)	0.03(1)	0.006(3)	0.009(3)	0.008(3)	0.03(1)	0.009(3)	0.008(3)
Na_2O	0.73(27)	0.04(1)	n.d.	n.d.	0.014(4)	0.02(1)	0.04(1)	0.02(1)	0.017(5)	0.02(1)	0.06(1)	0.04(1)	0.012(4)
MnO	2.21(30)	1.20(6)	1.04(8)	0.82(6)	0.67(3)	0.66(5)	0.81(5)	0.84(8)	0.81(6)	0.69(5)	1.93(4)	0.95(7)	0.76(5)
Cr_2O_3	1.61(34)	0.20(3)	0.12(3)	0.14(3)	0.15(2)	0.14(1)	0.13(1)	0.12(2)	0.21(3)	0.19(4)	0.41(2)	0.34(5)	0.81(8)
CdO	–	0.12(2)	n.d.	n.d.	0.06(2)	0.05(2)	0.08(2)	0.08(2)	0.14(4)	0.12(3)	0.29(3)	0.18(4)	–
TiO_2	0.12(3)	0.14(2)	0.09(2)	0.10(3)	0.09(1)	0.09(2)	0.11(2)	0.12(2)	0.18(4)	0.16(3)	0.22(2)	0.22(3)	0.22(4)
In_2O_3	–	0.07(2)	0.13(1)	0.12(1)	0.07(2)	0.07(2)	0.08(1)	0.07(1)	0.07(2)	0.06(1)	0.11(1)	0.09(2)	–
SO_3	0.01(1)	0.46(10)	1.46(31)	1.58(38)	1.63(35)	1.13(36)	1.28(22)	1.62(34)	0.92(35)	0.62(20)	0.26(3)	0.36(9)	0.02(1)
ZnO	–	0.41(3)	n.d.	n.d.	0.45(5)	0.39(4)	0.49(7)	0.37(3)	0.43(3)	0.34(3)	1.28(4)	0.68(6)	–
CuO	–	0.02(1)	n.d.	n.d.	0.03(1)	0.04(1)	0.04(1)	0.04(1)	0.04(1)	0.03(1)	0.03(1)	0.03(1)	–
Nb_2O_5	–	1.19(24)	n.d.	n.d.	0.57(14)	0.60(17)	0.61(24)	0.94(28)	1.14(29)	0.65(15)	1.26(12)	0.94(16)	–
Ta_2O_5	–	0.79(18)	n.d.	n.d.	0.36(11)	0.32(14)	0.39(21)	0.67(27)	0.85(26)	0.36(12)	0.72(7)	0.57(14)	–
SnO_2	–	0.01(1)	n.d.	n.d.	0.01(1)	0.01(1)	0.01(1)	0.005(4)	0.01(1)	0.008(5)	0.01(1)	0.009(4)	–
ZrO_2	0.13(5)	0.05(1)	n.d.	n.d.	0.02(1)	0.008(4)	0.03(1)	0.07(2)	0.05(2)	0.05(2)	0.02(1)	0.74(13)	0.01(1)
V_2O_3	2.19(44)	–	–	–	–	–	–	–	–	–	–	–	0.65(7)
P_2O_5	0.12(3)	–	–	–	–	–	–	–	–	–	–	–	0.04(1)
WO_3	0.04(2)	–	–	–	–	–	–	–	–	–	–	–	0.06(2)
Sum	98.83(65)	101.11(32)	99.96(62)	98.75(67)	102.00(42)	101.19(46)	100.33(51)	102.13(38)	101.49(51)	101.31(32)	97.10(69)	101.34(20)	101.61(30)
LA	*N = 14* *N (P) = 6* [e]	*N = 11*	*N = 15*	*N = 13*	*N = 12*	*N = 10*	*N = 13*	*N = 19*	*N = 13*	*N = 11*	*N = 15*	*N = 12*	*N = 12* *N (P) = 8*
CaO (wt%)	7.00(22)	8.02(73)	5.02(86)	3.63(48)	4.23(23)	4.50(18)	5.10(27)	5.68(55)	5.23(40)	6.06(59)	8.28(8)	6.93(30)	8.31(43)
P (ppm)	618(48)	–	–	–	–	–	–	–	–	–	–	–	161(7)
Ti	1074(27)	1218(98)	726(122)	564(83)	650(33)	786(28)	944(45)	817(100)	965(58)	1091(103)	1430(15)	1309(56)	1497(99)
V	14225(166)	–	–	–	–	–	–	–	–	–	–	–	–
Cr	10229(107)	1131(34)	879(240)	597(113)	910(94)	1169(63)	1044(53)	776(65)	990(116)	1115(86)	2742(18)	1805(68)	5335(114)
Mn	17180(222)	10105(462)	10097(1365)	5944(425)	5202(303)	5954(188)	6577(208)	6873(386)	5596(343)	5173(272)	15456(88)	6740(197)	6090(213)
Co	57(1)	–	–	–	–	–	–	–	–	–	–	–	94(2)
Ni	11.8(4)	–	–	–	–	–	–	–	–	–	–	–	23(1)
Cu	0.58(8)	222(12)	386(34)	322(35)	308(60)	460(108)	390(39)	295(36)	243(22)	288(32)	263(8)	292(15)	1.44(12)
Zn	18.4(4)	4186(215)	6433(1359)	3966(484)	4435(407)	4667(223)	5672(273)	4332(277)	3512(275)	3173(198)	12811(141)	5905(174)	29(1)
Ga	1.26(4)	2.15(21)	1.19(18)	0.79(11)	0.81(6)	0.95(6)	1.24(8)	1.30(14)	1.20(6)	1.75(11)	1.42(5)	1.59(9)	1.46(7)
Ge	10.9(4)	–	–	–	–	–	–	–	–	–	–	–	9.5(7)
Zr	1719(57)	394(38)	84(14)	326(44)	83(4)	95(4)	195(11)	552(59)	209(15)	268(33)	111(3)	4491(188)	30(3)
Nb	–	12284(1192)	11309(2038)	7969(1243)	5301(326)	6225(269)	7033(415)	7812(1063)	6752(483)	4619(497)	12452(334)	6355(293)	–
Mo	9.4(4)	–	–	–	–	–	–	–	–	–	–	–	15(1)
Cd	–	1519(123)	1127(127)	1041(162)	729(111)	1162(206)	1004(65)	884(93)	981(65)	979(58)	3564(57)	1608(60)	–
In	2.5(1)	735(49)	922(170)	756(69)	742(91)	1001(153)	841(57)	701(51)	667(68)	537(51)	1040(21)	908(29)	b.d.l.
Sn	0.16(3)	120(12)	146(29)	128(18)	139(24)	194(29)	161(15)	58(13)	117(21)	112(16)	137(5)	122(4)	0.18(2)
Ta	–	9419(936)	8241(1424)	5866(972)	4327(286)	4727(196)	7035(428)	6724(982)	5346(360)	3865(438)	9144(213)	4805(222)	–
W	416(16)	–	–	–	–	–	–	–	–	–	–	–	312(31)
Pb	1.09(6)	0.17(3)	0.63(10)	0.17(4)	0.09(2)	0.19(6)	0.42(11)	0.10(2)	0.11(1)	0.23(2)	0.61(8)	2.21(8)	0.53(6)

[a] *N* = number of measurements [b] Numbers in parentheses represent 2 SE [c] b.d.l. = below detection limit [d] n.d. = not determined [e] Number of measurements for P only

Table 11.3 *Composition of metallic melts as determined by EPMA and LA-ICP-MS.*

Run #	PR1490	PR1509	PR1519	PR1520	PR1523	PR1540	PR1556	PR1466	PR1467	PR1471	PR1478	PR1479	PR1482	PR1486
EPMA	*N = 25* [a]	*N = 9*	*N = 24*	*N = 34*	*N = 29*	*N = 27*	*N = 30*	*N = 35*	*N = 21*	*N = 30*	*N = 25*	*N = 31*	*N = 25*	*N = 29*
Fe (wt%)	88.15(63) [b]	82.42(125)	86.30(35)	88.96(52)	89.70(83)	84.04(106)	82.40(130)	69.50(119)	78.02(139)	74.48(82)	76.28(156)	77.48(101)	79.72(224)	79.90(434)
Si	0.95(2)	0.003(3)	0.005(4)	0.29(1)	0.009(3)	0.01(1)	0.008(3)	0.003(2)	0.008(3)	0.006(2)	0.011(5)	0.008(3)	0.005(2)	0.009(3)
S	0.02(4)	b.d.l.	0.004(3)	0.005(3)	0.008(3)	0.04(1)	0.009(5)	18.31(82)	13.93(95)	12.97(50)	14.70(99)	13,82(65)	13.76(154)	12.13(280)
Cr	0.11(1)	0.07(4)	0.17(1)	0.140(3)	0.027(5)	0.08(2)	0.03(1)	0.002(2)	0.012(3)	0.002(1)	0.011(4)	0.029(5)	0.011(3)	0.009(3)
Mn	0.01(1)	0.01(1)	0.017(9)	0.04(1)	0.004(2)	0.005(3)	0.009(5)	0.004(2)	0.024(5)	0.002(2)	0.062(5)	0.041(8)	0.045(11)	0.036(8)
Ni	4.18(6)	4.96(13)	4.80(8)	4.63(7)	3.67(7)	5.05(8)	5.12(8)	4.70(21)	0.011(6)	5.00(10)	0.02(1)	0.015(5)	0.008(4)	0.013(6)
Cu	–	–	–	–	–	–	–	0.12(2)	1.54(10)	0.10(1)	1.81(15)	1.56(9)	1.17(20)	1.49(34)
Zn	–	–	–	–	–	–	–	–	0.54(5)	–	0.51(7)	0.66(7)	1.07(50)	0.38(6)
As	0.84(3)	1.42(9)	1.06(4)	1.24(8)	0.63(3)	1.51(5)	1.49(4)	n.d. [c]	–	n.d.	–	–	–	–
Se	0.53(11)	1.72(32)	0.094(16)	0.30(8)	0.82(27)	2.06(25)	2.26(33)	n.d.	–	n.d.	–	–	–	–
Cd	0.24(9)	0.30(13)	0.012(8)	0.44(14)	0.30(13)	0.82(15)	1.14(24)	0.61(10)	1.07(17)	0.55(10)	1.22(13)	1.28(14)	1.04(41)	1.22(40)
In	1.39(18)	2.05(28)	0.44(3)	1.35(17)	1.24(26)	1.66(18)	1.95(22)	0.76(10)	1.71(25)	1.11(9)	2.33(23)	1.96(15)	1.50(30)	1.75(56)
Sn	–	–	–	–	–	–	–	–	1.07(7)	–	1.38(11)	1.32(6)	0.55(18)	1.34(25)
Sb	2.35(19)	2.55(22)	1.86(4)	1.96(19)	1.15(6)	2.48(21)	2.44(20)	n.d.	–	n.d.	–	–	–	–
Te	0.16(3)	0.90(16)	0.032(13)	0.25(7)	0.51(13)	1.40(17)	1.62(20)	n.d.	–	n.d.	–	–	–	–
Pb	0.33(8)	0.79(14)	0.039(17)	0.61(16)	0.35(11)	1.13(15)	1.56(21)	n.d.	–	n.d.	–	–	–	–
Sum	99.26(29)	97.25(115)	94.82(29) [d]	100.20(8)	98.41(15)	100.84(10)	100.03(31)	94.07(37)	97.96(20)	94.25(26)	98.37(31)	98.19(26)	98.89(22)	98.30(37)
LA	*N = 6*	*N = 10*	*N = 3*	*N = 12*	*n.a.* [g]	*N = 10*	*N = 11*	*N = 10*	*N = 10*	*N = 10*	*N = 14*	*N = 11*	*N = 7*	*N = 8*
Si (ppm)	7151(1034)	b.d.l.	b.d.l.	3489(118)	–	b.d.l.	b.d.l.	423(125)	464(109)	b.d.l.	b.d.l.	732(55)	b.d.l.	b.d.l.
Ti	b.d.l. [e]	b.d.l.	b.d.l.	b.d.l	–	b.d.l.	b.d.l.	5.5(7)	b.d.l.	b.d.l.	b.d.l.	b.d.l.	b.d.l.	b.d.l.
Cr	1017(89)	708(113)	1124(96)	1234(20)	–	1299(136)	524(64)	53(23)	255(63)	b.d.l.	259(49)	451(24)	199(77)	b.d.l.
Mn	232(30)	57(8)	77(43)	441(11)	–	153(29)	50(6)	49(9)	695(120)	19(3)	939(84)	538(31)	687(241)	526(79)
Ni	*Int.* [f]	*Int.*	*Int.*	*Int.*	–	*Int.*	*Int.*	*Int.*	134(20)	*Int.*	271(32)	179(2)	100(22)	114(18)
Cu	142(11)	81(7)	71(15)	88(2)	–	290(19)	90(6)	353(33)	*Int.*	269(37)	*Int.*	*Int.*	*Int.*	*Int.*
Cu_{corr}	93(7)	53(5)	46(10)	57(1)	–	189(12)	59(4)	229(21)	–	175(24)	–	–	–	–
Zn	1981(335)	87(6)	b.d.l.	97(4)	–	202(21)	66(4)	23(3)	21501(7262)	21(3)	13798(3208)	17177(1244)	36726(15024)	19366(1871)
Zn_{corr}	476(80)	21(1)	–	23(1)	–	48(5)	16(1)	8(1)	5160(148)	7(1)	3312(770)	4122(299)	8814(3606)	4648(1057)
Ga	4.2(9)	2.9(3)	b.d.l.	2.7(2)	–	4.3(3)	3.6(1)	1.6(3)	2.6(11)	2.0(3)	4.6(12)	3.8(3)	14(4)	3.4(11)
Ga_{corr}	3.2(7)	2.3(3)	–	2.1(2)	–	3.3(3)	2.8(1)	1.2(3)	2.0(9)	1.5(3)	3.5(9)	2.9(2)	11(4)	2.6(9)
As	8918(358)	13878(365)	11373(923)	12643(523)	–	21490(968)	15554(229)	7653(340)	–	8034(384)	–	–	–	–
Se	11011(1280)	21282(2579)	1601(399)	4739(282)	–	39361(3501)	25055(2632)	14105(1003)	–	16247(891)	–	–	–	–
Se_{corr}	7928(922)	15323(1857)	1153(287)	3412(203)	–	28700(2521)	18040(1895)	10156(722)	–	11698(642)	–	–	–	–
Nb	–	–	–	–	–	–	–	0.35(3)	0.91(39)	0.39(3)	b.d.l.	0.35(8)	1.26(57)	1.62(38)
Cd	19590(2998)	33076(15444)	1602(931)	35601(2902)	–	68770(10322)	48923(4711)	17501(2173)	44603(10232)	28082(1897)	47118(11041)	48181(3014)	65812(18167)	92934(7287)
Cd_{corr}	2743(420)	4631(2162)	224(130)	4984(406)	–	9628(1445)	6849(660)	2450(304)	6244(1432)	3931(266)	6597(1546)	6745(422)	9214(2543)	13011(1020)
In	32169(3653)	30332(4108)	6976(1345)	28047(1934)	–	47957(4116)	30029(3056)	13263(990)	29088(3207)	17559(1029)	34833(4167)	29745(671)	27199(3852)	41356(5433)
In_{corr}	15763(1790)	14863(2013)	3418(659)	13743(948)	–	23499(2017)	14714(1497)	6499(485)	14253(1571)	8604(504)	17068(2042)	14575(329)	13328(1887)	20264(2662)
Sn	134(11)	5.5(4)	25(1)	5.4(5)	–	103(7)	7.0(6)	25(1)	16138(2305)	18(1)	20138(2433)	17626(265)	7121(2738)	22289(2268)
Sn_{corr}	98(8)	4.0(3)	19(1)	3.9(4)	–	75(5)	5.1(4)	18(1)	11781(1683)	13(1)	14701(1776)	12867(191)	5198(1999)	16271(1656)
Sb	34844(1472)	26262(1487)	23485(1820)	23048(791)	–	37515(2585)	27022(1284)	14819(895)	–	14053(1006)	–	–	–	–
Sb_{corr}	25785(1089)	19434(1100)	17379(1347)	17056(585)	–	27835(1913)	19996(950)	10966(662)	–	10399(744)	–	–	–	–
Te	6011(854)	21158(4703)	1864(1042)	8767(609)	–	50442(4379)	30409(2715)	18984(1604)	–	17764(1197)	–	–	–	–
Te_{corr}	2344(333)	8252(1834)	727(406)	3419(238)	–	19572(1708)	11860(1059)	7404(626)	–	6928(467)	–	–	–	–
Ta	–	–	–	–	–	–	–	–	–	–	var.	0.042(9)	0.08(2)	0.10(5)
Pb	13536(1220)	18990(8174)	849(806)	29932(3763)	–	41798(5158)	25641(2995)	8705(814)	6.7(17)	18799(1413)	36(6)	11.5(3)	8.6(41)	9.9(14)
Pb_{corr}	4873(439)	6836(2943)	306(290)	10776(1355)	–	15047(1857)	9231(1078)	3134(293)	2.4(6)	6768(509)	13(2)	4.1(1)	3.1(15)	3.6(5)

Run #	PR1487	PR1488	PR1503	PR1504	PR1529	PR1530	PR1531	PR1537	PR1548	PR1549	PR1551	PR1557	PR1560
EPMA	*N = 25*	*N = 30*	*N = 12*	*N = 8*	*N = 26*	*N = 29*	*N = 36*	*N = 36*	*N = 30*	*N = 29*	*N = 25*	*N = 30*	*N = 25*
Fe (wt%)	92.96(50)	84.41(7)	76.84(149)	74.30(202)	78.83(87)	79.43(103)	77.63(99)	87.36(106)	79(102)	81.04(169)	79.08(103)	78.82(149)	91.09(16)
Si	b.d.l.	0.012(3)	0.008(2)	0.005(2)	0.007(3)	0.006(3)	0.010(5)	0.009(4)	0.006(2)	0.005(2)	0.006(2)	0.008(4)	b.d.l.

P	0.41(11)	–	–	–	–	–	–	–	–	–	–	–	0.64(5)
S	0.015(4)	9.26(6)	12.17(103)	13.11(138)	12.26(63)	11.15(74)	13.75(70)	8.82(77)	13.07(78)	13.08(126)	13.46(66)	14.44(108)	0.03(1)
V	0.09(1)	–	–	–	–	–	–	–	–	–	–	–	0.02(1)
Cr	0.45(2)	0.011(3)	0.03(2)	0.06(2)	0.015(3)	0.015(4)	0.004(2)	0.013(3)	0.06(5)	0.007(4)	0.07(4)	0.007(3)	0.12(3)
Mn	0.06(1)	0.018(4)	0.04(2)	0.03(1)	0.10(1)	0.043(5)	0.07(1)	0.06(1)	0.04(1)	0.019(6)	0.04(1)	0.010(4)	0.014(7)
Co	1.11(2)	–	–	–	–	–	–	–	–	–	–	–	1.61(1)
Ni	0.57(1)	0.016(5)	b.d.l.	b.d.l.	0.008(4)	0.02(1)	0.015(5)	0.012(4)	0.010(5)	0.012(5)	0.009(5)	0.031(8)	1.41(2)
Cu	–	1.36(2)	n.d.	n.d.	1.73(8)	1.81(8)	1.75(10)	0.66(6)	1.61(11)	1.64(21)	1.47(11)	1.48(14)	–
Zn	–	0.025(9)	n.d.	n.d.	0.58(7)	0.53(7)	0.39(5)	0.36(20)	0.47(5)	0.30(2)	0.62(8)	0.21(2)	–
Ge	0.53(3)	–	–	–	–	–	–	–	–	–	–	–	1.51(2)
Mo	0.47(8)	–	–	–	–	–	–	–	–	–	–	–	1.71(8)
Cd	–	0.19(2)	1.09(22)	1.00(35)	1.14(15)	1.35(18)	1.12(14)	0.45(29)	1.54(21)	1.10(24)	1.30(15)	1.24(35)	–
In	–	1.45(2)	2.14(17)	1.84(37)	2.16(14)	2.10(13)	2.14(15)	1.15(13)	1.93(17)	1.35(23)	1.84(20)	1.78(23)	–
Sn	–	1.58(2)	n.d.	n.d.	1.39(9)	1.74(8)	1.41(7)	0.08(1)	1.50(10)	1.32(16)	1.41(11)	1.42(14)	–
W	1.49(15)	–	–	–	–	–	–	–	–	–	–	–	1.47(3)
Sum	98.15(22)	98.36(10)	92.51(97)	90.59(104)	98.25(19)	98.21(20)	98.32(23)	98.99(13)	98.25(21)	99.91(17)	99.33(19)	99.50(25)	99.64(12)
LA	*n.a.*	*n.a.*	*n.a.*	*n.a.*	*N = 11*	*N = 10*	*N = 13*	*n.a.*	*N = 5*	*N = 8*	*N = 14*	*N = 9*	*N = 10* *N (P) = 6* [h]
Si (ppm)	–	–	–	–	b.d.l.	b.d.l.	b.d.l.	–	b.d.l.	b.d.l.	b.d.l.	b.d.l.	b.d.l.
P	–	–	–	–	–	–	–	–	–	–	–	–	7397(398)
Ti	–	–	–	–	b.d.l.	b.d.l.	b.d.l.	–	b.d.l.	b.d.l.	b.d.l.	b.d.l.	b.d.l.
V	–	–	–	–	–	–	–	–	–	–	–	–	284(74)
V_{corr}	–	–	–	–	–	–	–	–	–	–	–	–	395(103)
Cr	–	–	–	–	330(38)	204(22)	166(24)	–	147(52)	67(42)	1444(111)	434(173)	2512(634)
Mn	–	–	–	–	1563(112)	473(103)	947(71)	–	583(101)	388(60)	811(60)	361(115)	361(66)
Co	–	–	–	–	–	–	–	–	–	–	–	–	14280(110)
Ni	–	–	–	–	182(7)	221(21)	122(15)	–	162(59)	165(9)	139(3)	441(13)	*Int.*
Cu	–	–	–	–	*Int.*	*Int.*	*Int.*	–	*Int.*	*Int.*	*Int,*	*Int.*	45(2)
Cu_{corr}	–	–	–	–	–	–	–	–	–	–	–	–	29(1)
Zn	–	–	–	–	17842(1667)	14158(1313)	35079(2454)	–	30780(5003)	8256(492)	15759(1006)	7528(1244)	57(8)
Zn_{corr}	–	–	–	–	4282(400)	3398(315)	8419(589)	–	7387(1201)	1981(118)	3782(241)	1807(298)	14(2)
Ga	–	–	–	–	3.9(3)	4.8(7)	4.9(5)	–	3.7(5)	6.4(6)	2.8(1)	3.4(4)	5.5(5)
Ga_{corr}	–	–	–	–	3.0(2)	3.7(6)	3.8(4)	–	2.9(4)	4.9(5)	2.2(1)	2.6(4)	4.2(4)
Nb	–	–	–	–	4.1(11)	0.93(50)	2.2(4)	–	b.d.l.	21(16)	117(22)	17(8)	–
Cd	–	–	–	–	48613(3697)	52551(4760)	108879(6230)	–	140430(13238)	46734(7487)	50441(3176)	45276(5231)	–
Cd_{corr}	–	–	–	–	6806(518)	7357(666)	15243(872)	–	19660(1853)	6543(1048)	7062(445)	6339(732)	–
In	–	–	–	–	34460(625)	32232(2187)	44316(12297)	–	44762(7745)	23392(1423)	28237(352)	28688(977)	b.d.l.
In_{corr}	–	–	–	–	16885(306)	15794(1072)	21715(6026)	–	21933(3795)	11462(697)	13836(172)	112057(479)	–
Sn	–	–	–	–	19974(521)	25536(2029)	22627(924)	–	24193(4315)	17626(694)	18701(328)	19767(341)	10.5(6)
Sn_{corr}	–	–	–	–	14581(380)	18714(1481)	16518(675)	–	17661(3150)	12867(507)	13652(239)	14430(285)	7.6(4)
Ta	–	–	–	–	0.08(2)	0.030(3)	0.09(3)	–	b.d.l.	0.70(32)	2.3(6)	2.0(13)	–
Pb	–	–	–	–	7.6(9)	9.1(7)	35(2)	–	16(5)	16(1)	5.1(1)	132(9)	13(2)
Pb_{corr}	–	–	–	–	2.7(3)	3.3(3)	13(1)	–	5.8(20)	5.8(3)	1.84(4)	48(3)	4.7(6)

[a] *N* = number of measurements [b] Numbers in parentheses represent 2 SE [c] n.d. = not determined [d] Low total of metal phase is most likely due to C contamination from the graphite heater [e] b.d.l. = below detection limit [f] Used as internal standard for LA-ICP-MS processing [g] Not analysed [h] Number of measurements for P only

11.3.2 Effect of temperature on metal-silicate partitioning

11.3.2.1 Volatile elements S, Se, Te

To isolate the effect of temperature on the metal-silicate partitioning behavior of S, Se and Te, we consider the partitioning data that was obtained at a constant pressure of ~3.8 GPa and correct D values for variable FeO contents of the silicate melts using the expressions reported in Steenstra et al. (2017c). Figure 11.2 shows the metal-silicate partition coefficients of S, Se and Te at ~3.8 GPa, normalized to $x_{\mathrm{FeO}}^{\mathrm{silicate}}$ = 0.10, as a function of temperature across the experimental range of 1973–2873 K. The results show that temperature decreases the siderophile behavior of all three elements considered, but the magnitudes vary for each element. Sulfur partitioning is least affected by temperature, with a decrease of its log D value by ~0.75 between 1973 and 2873 K. The log D values of Se and Te are more strongly affected by temperature and decrease by ~1.55 and ~2 log units across the studied temperature range, respectively. However, the correlation between temperature and variable silicate melt compositions in our experiments is significant and could be responsible for a significant fraction of the observed variability of their D values with temperature. We tested this hypothesis by comparing experimental data with similar MgO contents of the silicate melts. This approach yields a similar decrease of log D values with temperature, suggesting the decrease of $\mathrm{D}_{\mathrm{S,\ Se,\ Te}}^{\mathrm{met-sil}}$ values is predominantly not the result of variations in silicate melt compositions. This is consistent with thermodynamic data for the behavior of S in silicate melts. Assuming the sulfide capacity terms derived for S (O'Neill and Mavrogenes, 2002) are also valid for Se and Te (Rose-Weston et al., 2009), variable silicate melt compositions can only explain a variation of up to ~0.2 log units for the metal-silicate partition coefficients for S, Se and Te derived here.

Our results for S, Se and Te are broadly consistent with previous studies. Rose-Weston et al. (2009), Boujibar et al. (2014) and Suer et al. (2017) argued that S behaves less siderophile with increasing temperature. Published thermodynamic models also predict an increase in the solubility of S in silicate melts with increasing temperature (Mavrogenes and O'Neill, 1999; Holzheid and Grove, 2002; Liu et al., 2007; Ding et al., 2017; Smythe et al., 2017; Steenstra et al., 2018b). Rose-Weston et al. (2009) argued for a similar decrease of the siderophile behavior of S, Se, Te with increasing temperature. Steenstra et al. (2017c) did not identify significant temperature effects on the metal-silicate partitioning behavior of S, Se and Te over the temperature range of ~1800–2300 K. Empirical parameterizations obtained for Se and Te also did not yield a significant temperature term (Steenstra and van Westrenen, 2018). These discrepancies are most likely due to the more limited temperature range of the experimental datasets that were considered in this previous study.

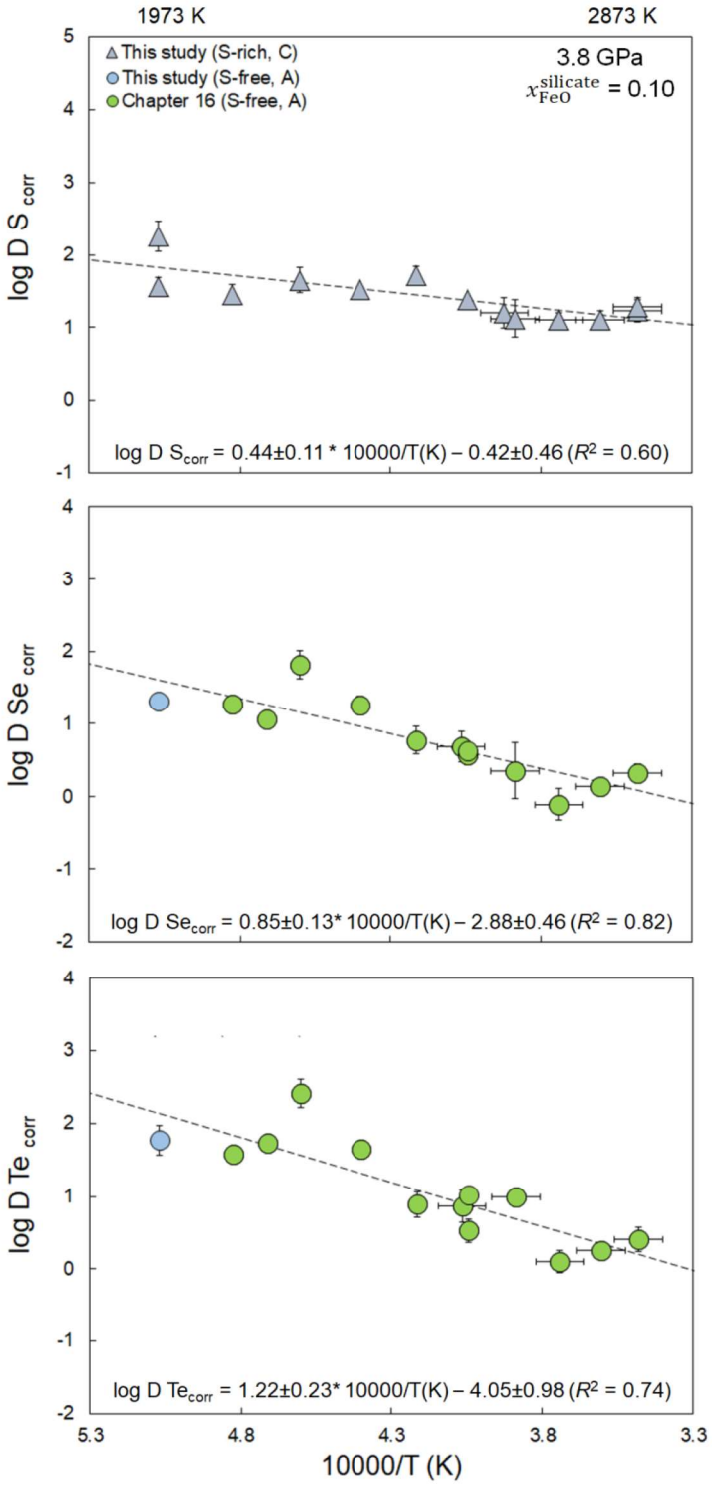

Fig. 11.2 *The effects of temperature within the range of 1973–2873 K on $D_{S,\ Se,\ Te}^{met-sil}$ at a constant pressure of ~3.8 GPa, based on data from this study and Chapter 16. All values were corrected to a common $x_{FeO}^{silicate}$ value of 0.10, using the silicate melt compositional dependencies reported in Steenstra et al. (2017c). Letters denote type of metal mixture used. Errors represent propagated errors based on 2 SE for EPMA and/or LA-ICP-MS derived concentration. Dotted line represents best fit to the data.*

11.3.2.2 Volatile elements Cu, Zn, Ga, Ge, Cd, Sn, In, Pb

Fig. 11.3 shows the metal-silicate partition coefficients of Cu, Zn and Ga from this study and Chapter 16, normalized to ΔIW = –2, as a function of temperature. The metal-silicate partition coefficients of Cu decrease slightly with increasing temperature (Fig. 11.3). Note that the temperature effects for Cu partitioning into S-free and S-rich alloys are very similar, and correspond to a decrease of approximately 0.15 log units between 1973 and 2873 K. A decrease of the siderophile behavior of Cu is consistent with the experimental results of Holzheid and Lodders (2001), Corgne et al. (2008) and Righter et al. (2010) obtained at lower temperatures (1573–2473 K). It is also consistent with an empirical equation describing its metal-silicate partitioning behavior based on a literature compilation of prior partitioning studies (Steenstra et al., 2016b). As demonstrated in Corgne et al. (2008), a decrease of $D_{Cu}^{met-sil}$ with temperature is in agreement with 1 bar free energy data for Cu (Barin et al., 1989). Our results disagree with the strongly positive effects of temperature on metal-silicate partitioning of Cu suggested from the empirical parameterization reported by Yang et al. (2015). The positive offset of $D_{Cu}^{met-sil}$ by ~ –0.8 units for S-rich experiments is consistent with the chalcophile nature of Cu (Wood et al., 2014).

Log $D_{Zn}^{met-sil}$ increases with increasing temperature (Fig. 11.3), by 0.25 to 0.65 across a temperature range of 900 degrees. The increasingly siderophile behavior of Zn with increasing temperature is consistent with most previous experimental studies (Corgne et al., 2008; Righter et al., 2010; Siebert et al., 2011; Ballhaus et al., 2013; Mahan et al., 2017). We note that the parameterization for $D_{Zn}^{met-sil}$ of Yang et al. (2015) suggests Zn should behave significantly less siderophile with increasing temperature, which is also inferred from 1 bar free energy data for ZnO (Siebert et al., 2011). This discrepancy may be due to significant uncertainties in the underlying thermodynamic parameters required for calculating these values (Siebert et al., 2011). Our results confirm that the siderophile behavior of Zn is only slightly affected by addition of S to the metal phase (Wood et al., 2014; Chapter 5).

Consideration of the results for both S-free and S-rich experiments shows an increase of $D_{Ga}^{met-sil}$ with temperature (Fig. 11.3). The increase of $D_{Ga}^{met-sil}$ with temperature is significant for S-free experiments and near-negligible for S-rich systems but overall log $D_{Ga}^{met-sil}$ values for S-rich systems are similar to those for S-free systems. Literature estimates of the effect of temperature on $D_{Ga}^{met-sil}$ vary considerably. Mann et al. (2009) reported a lack of consistent effects of temperature on Ga metal-silicate partitioning. Both Corgne et al. (2008) and Siebert et al. (2011) argued from experimental partitioning data and thermodynamic models based on 1

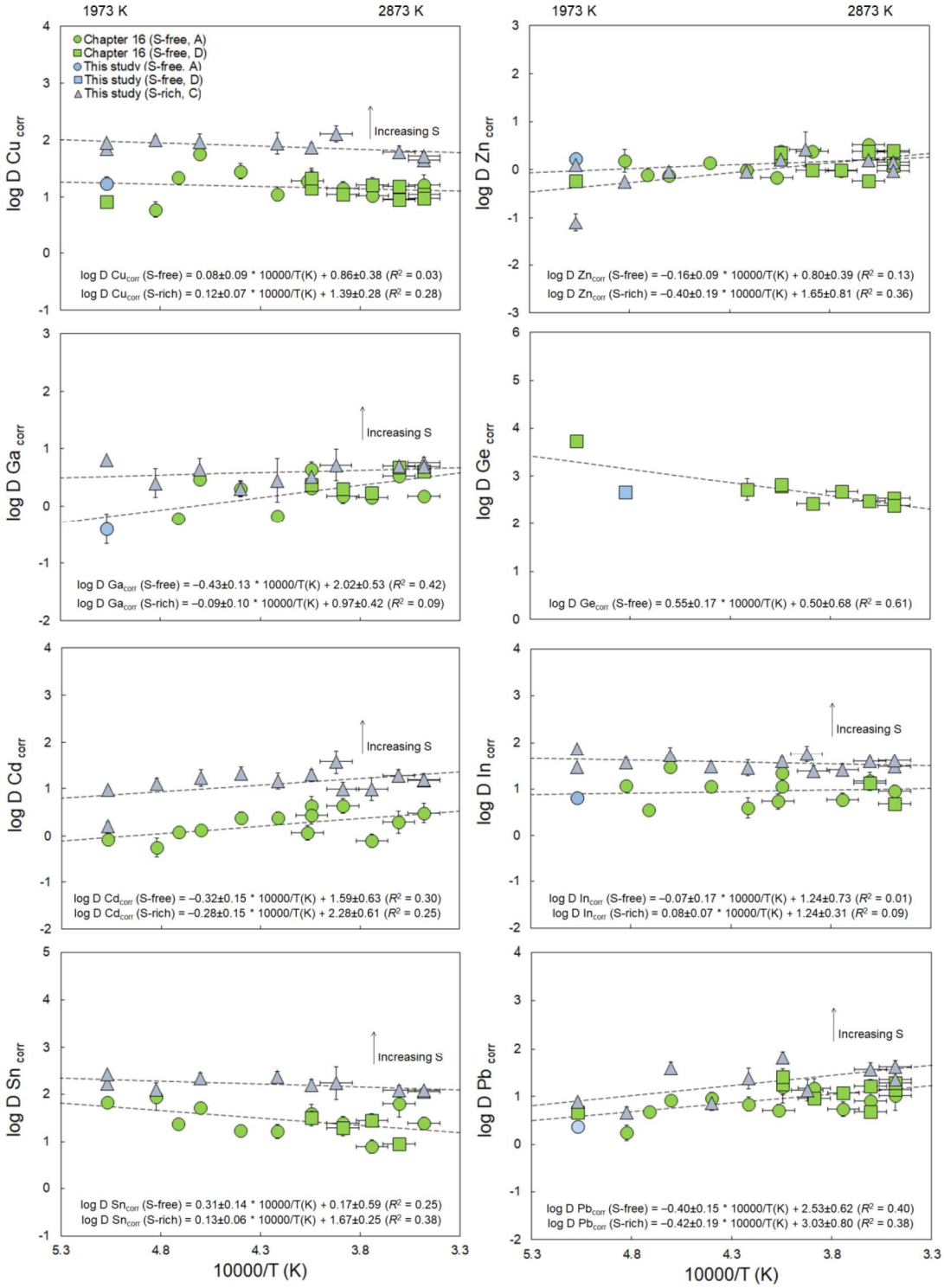

Fig. 11.3 *The effects of temperature on the metal-silicate partitioning behavior of Cu, Zn, Ga, Ge, Cd, In, Sn and Pb at a constant pressure of ~3.8 GPa. Data from this study and Chapter 16. Letters denotes type of metal mixture used. All values were corrected to ΔIW = –2 assuming a 1+ valence state for Cu, 2+ for Zn, Ge, Cd, Sn, Pb and 3+ for Ga and In. Errors represent propagated errors based on 2 SE for EPMA and/or LA-ICP-MS derived concentrations. Dotted line represents best fit to the data.*

bar free energy data that Ga behaves more siderophile with increasing temperature. Righter et al. (2010) reported a decrease of $D_{Ga}^{met-sil}$ with temperature, although this was based on a comparatively narrow temperature range of 400 K. Blanchard et al. (2015) concluded temperature is not a statistically significant parameter affecting $D_{Ga}^{met-sil}$. Yang et al. (2015) argued for strongly negative temperature effects on the metal-silicate partitioning behavior of Ga, based on a compilation of metal-silicate partitioning data. Finally, Steenstra et al. (2016a,b) reported empirical parameterizations for Ga that predict its siderophile behavior should increase with temperature, consistent with the results found here. According to the results of Wood et al. (2014) and Blanchard et al. (2015), Ga should behave less siderophile with increasing S, but this is not evident from our data.

Germanium shows a modest decrease of its siderophile behavior with increasing temperature (Fig. 11.3). Previous studies generally reported negative effects of temperature as well. Siebert et al. (2011) and Righter et al. (2011c, 2018a) used metal-silicate partitioning data to argue for a decrease of $D_{Ge}^{met-sil}$ with temperature. However, it should be noted that this effect is opposite to what would be expected from consideration of 1 bar free energy data for Ge (Siebert et al., 2011).

The metal-silicate partition coefficients of volatile element Cd increase substantially with temperature, reflected by a consistent increase of log $D_{Cd}^{met-sil}$ by 0.4 and 0.5 log units across the temperature range of 1973–2873 K for S-rich and S-free systems, respectively (Fig. 11.3). A similar increase in both systems is observed for $D_{Pb}^{met-sil}$ (Fig. 11.3). The log $D_{Pb}^{met-sil}$ values increase by 0.6 log units across the considered temperature range. Positive effects of temperature on $D_{Cd,\ Pb}^{met-sil}$ have been proposed previously (Wood and Halliday, 2010; Ballhaus et al., 2013; Bouhifd et al., 2013; Righter et al., 2018a). Our new results also confirm that both Cd and Pb behave chalcophile (Wood et al., 2008b; 2014; Chapter 5).

The siderophile behavior of In and Sn remains constant or slightly decreases with increasing temperature (Fig. 11.3), which agrees with previous studies (Mann et al., 2009; Ballhaus et al. 2013; Righter et al., 2018a). This observation is also in agreement with the reported lack of a significant temperature term for $D_{Sn}^{met-sil}$ (Steenstra et al., 2017b). Our data suggests both In and Sn also behave chalcophile, with higher $D_{In,\ Sn}^{met-sil}$ values for S-rich systems. The latter is consistent with the findings of Wood et al. (2014) for In, but disagrees with preliminary results of Ballhaus et al. (2017) for Sn.

11.3.2.3 Volatile and refractory elements P, As, Mo, Sb, W

For higher valence volatile elements P, As, Sb and refractory elements Mo and W assessment of the effects of temperature on their metal-silicate portioning is complicated by the evolution of silicate melt compositions with increasing experimental run temperatures due to progressive interaction with the MgO capsules. It is widely established that their metal-silicate partitioning behavior is highly sensitive to changes in silicate melt compositions (e.g. O'Neill and Eggins, 2002; Righter et al., 2009b, 2010; Siebert et al., 2011; Steenstra et al., 2017b; Chapter 5). In our new experiments, this is particularly evident from the significant offset of $D_{P,\ Mo,\ W}^{met-sil}$ values of run PR1538. In this experiment, silicate melt CaO and Al_2O_3 concentrations are approximately twice as high as for the other experiments due to crystallization of forsterite and less MgO enrichment of the silicate melt, resulting in much higher $D_{P,\ Mo,\ W}^{met-sil}$ values than would be expected given their observed dependencies on temperature (Fig. 11.4). Due to these complexities, temperature trends will likely be a combination of the effects of variable silicate melt composition and direct temperature effects. Despite these issues, our results reproduce the increase in the siderophile behavior of P and W with increasing temperatures and the decrease of $D_{As,\ Mo,\ Sb}^{met-sil}$ (Fig. 11.4) observed for experiments performed in graphite capsules with (near)-constant silicate melt compositions by other workers (Righter et al., 2009b; Siebert et al., 2011).

11.3.3 Effects of pressure on metal-silicate partitioning of volatile elements

To assess the effects of pressure on partitioning at high temperature, we performed a pressure series at constant temperature and for near-constant metal compositions (this study; Chapter 16). Fig 11.5 shows the effects of pressure on the metal-silicate partitioning of S, Se and Te at constant temperature. Our results yield positive pressure dependencies for all three elements, which are within error of those we have previously derived at lower pressures using a piston cylinder press (1–2.5 GPa; Steenstra et al., 2017c). Copper also behaves significantly more siderophile with increasing pressure (Fig. 11.5). This is in contrast with the results of Corgne et al. (2008), who found no evidence for a pressure dependency of $D_{Cu}^{met-sil}$. For the other VSE, no significant or consistent pressure trends were observed. The latter is most likely due to the relatively narrow pressure range that is studied and the overall lack of significant pressure effects on their partitioning as previously shown for several of these elements (Siebert et al., 2011; Righter et al., 2018a).

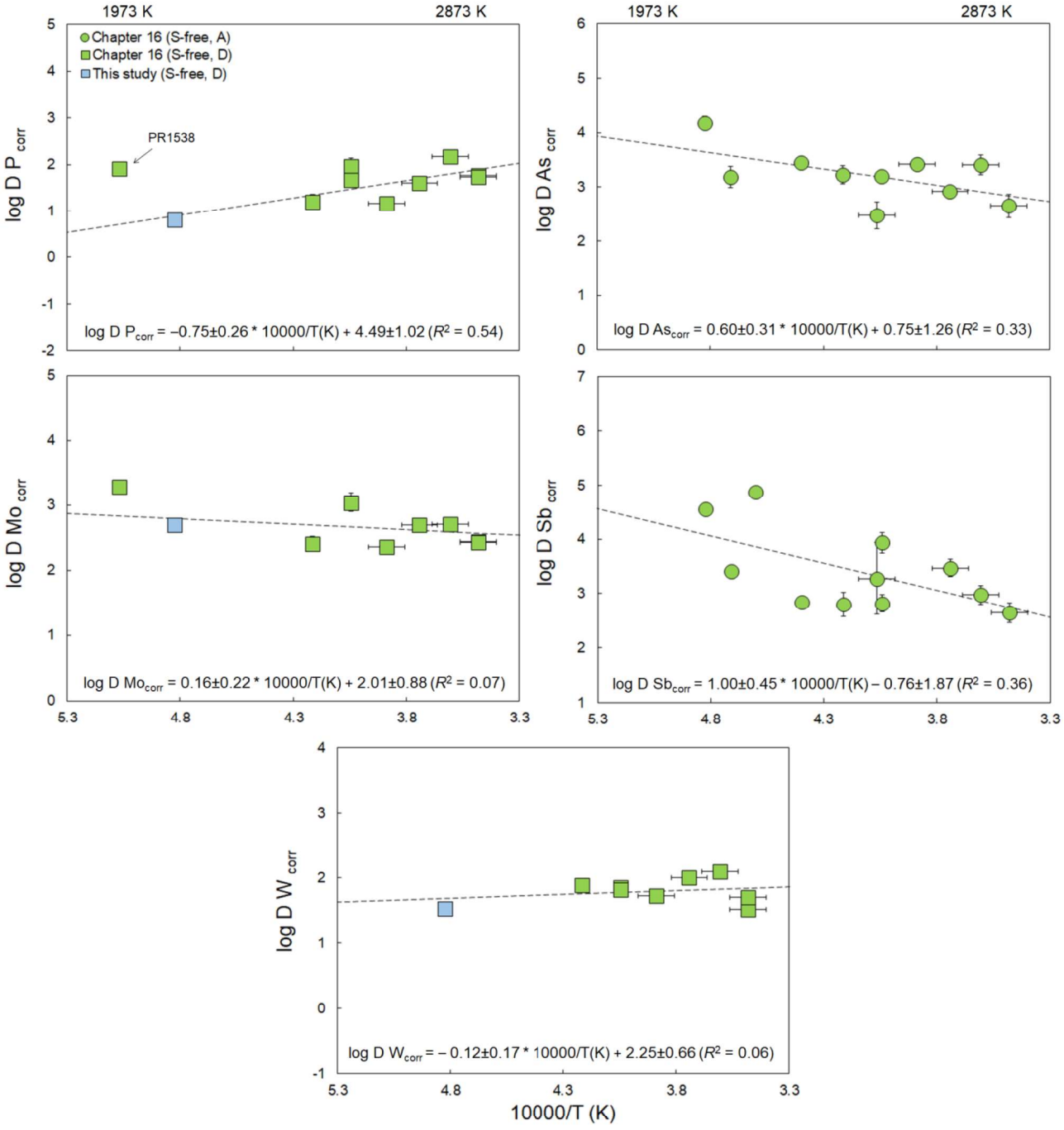

Fig. 11.4 *The effects of temperature within the range of 1973–2873 K on the metal-silicate partition coefficients of P, As, Mo, Sb and W at a constant pressure of ~3.8 GPa, based on data from this study and Chapter 16. Metal-silicate partition coefficients were corrected to ΔIW = –2 assuming a 3+ valence state for Sb, 4+ for Mo, 5+ for P, As and 6+ for W. Data points for run PR1538 were excluded from fit for P and W given the significantly different Al_2O_3 and CaO concentrations of the silicate melt and corresponding effects on the activity coefficient of P and W in silicate melts (Steenstra et al., 2017b). Letters denote type of metal mixture used. Errors represent propagated errors based on 2 SE for EPMA and/or LA-ICP-MS derived concentrations. Dotted line represents best fit to the data.*

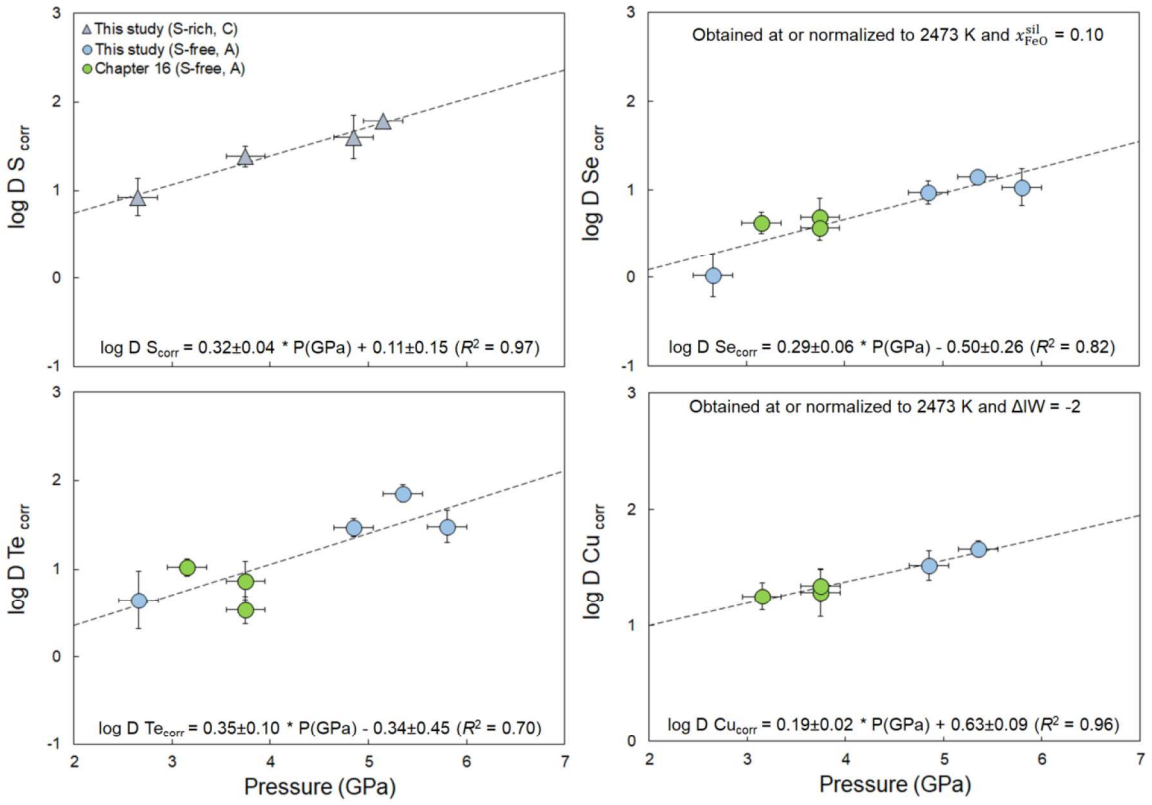

Fig. 11.5 *The effects of pressure on the metal-silicate partition coefficients of S, Se, Te and Cu at 2473 K based on data from this study and Chapter 16. The $D_{S,\ Se,\ Te}^{met-sil}$ values were normalized to a common $x_{FeO}^{silicate}$ value of 0.10, according to the dependencies reported in Steenstra et al. (2017c). The $D_{Cu}^{met-sil}$ values were corrected to ΔIW = –2 assuming a 1+ valence state of Cu. The $D_{S}^{met-sil}$ values of runs PR1549 and PR1557 were normalized to 2473 K using the temperature trend derived in this study. Letters denote type of metal mixture used. Errors represent propagated errors based on 2 SE for EPMA and/or LA-ICP-MS derived concentrations. Dotted line represents best fit to the data.*

11.4 IMPLICATIONS

11.4.1 Effect of high-temperature core formation on volatile element depletions

In previous studies, it was noted that many volatile elements (e.g. P, Zn, Cu Sb, Ge, Cd, In, S, Se, Te, Pb) can be segregated from silicate melt through their preferential partitioning in to metal or sulfide phases (e.g. Wood and Halliday, 2010; Bouhifd et al., 2013; Yang et al., 2015; Righter et al., 2017b; 2018a,b; Steenstra et al., 2017c, Steenstra and Westrenen, 2018; Chapters 5, 7). In this section we re-assess the potential of volatile element storage in the cores of Mars and the Moon, in light of the new experimental constraints obtained in this study.

To assess whether volatile element depletions in the lunar and martian mantle can be reconciled with core formation, we use Eq. 3.7 to calculate their required metal-silicate partition coefficients. The required log D values for Mars were calculated using the bulk Mars estimates of Lodders and Fegley (1997) and Sanloup et al. (1999) and the bulk silicate Mars abundances

proposed by Taylor (2013) and Wang and Becker (2017) (Table 11.4). For the Moon, we assume that the bulk silicate Earth (BSE) is representative of the composition of the bulk Moon (Table 11.4). A highly degree of similarity between the BSE and bulk Moon is implied from current models of lunar formation (Canup, 2012; Ćuk and Stewart, 2012; Lock et al., 2018) and from major and minor elemental and isotopic compositions of primitive lunar and terrestrial materials (e.g. Warren, 2005; Zhang et al., 2012; Dauphas et al., 2014; Taylor and Wieczorek, 2014; Warren and Dauphas, 2014; Young et al., 2016; Warren and Siegler, 2016; Sossi and Moynier, 2017).

Table 11.4 *Abundances of volatile elements in bulk Mars and Moon and silicate Mars and Moon and the corresponding log D values needed to explain mantle depletions by core formation. The required log D values were calculated for a martian and lunar core mass range of 21 to 28 and 1 to 2.5 mass%, respectively, using Eq. 3.7.*

	bulk Mars[a]	bulk silicate Mars[b]	required log D	bulk Moon (BSE)[c]	bulk silicate Moon[d]	required log D
S (ppm)	34300±12300	360±120	2.96±0.38	250±50	79±16	2.24±0.46
P	1412±312	675±215	0.71±0.44	82±8	57±12	1.30±0.71
Cu	121±34	4.5±2.5	2.09±0.47	28±4	7.2±1.4	2.26±0.40
Zn	128±62	44±26	0.76±0.90	54±3	7.7±1.5	2.59±0.33
Ga	10±3	7±3	<1.07	4.3±0.2	2.3±0.5	1.74±0.44
Ge	24±9	1.38±1.13	2.04±0.76	1.14±0.12	0.015±0.003	3.68±0.33
As (ppb)	2515±515	45±40	2.69±0.77	606±150	120±24	2.39±0.45
Se	14330±5830	100±27	2.75±0.37	80±17	24±5	2.17±0.41
Cd	212±132	17±13	1.73±0.88	38±6	12±2.4	2.12±0.43
In	30±14	10±5	0.84±0.74	13±2	1.6±0.3	2.65±0.37
Sn	867±49	240±210	1.37±0.90	118±19	39±8	2.10±0.44
Sb	154±78	200±100	<0.86	5.7±1.6	0.08±0.02	3.64±0.44
Te	1035±605	0.50±0.25	3.99±0.50	11±1.7	4.1±0.8	2.04±0.40
Pb	-	-	-	167±14	28±6	2.51±0.35

[a] bulk Mars estimates based on proposed bulk Mars models of Lodders and Fegley (1997) and Sanloup et al. (1999), in conjunction with the compiled trace element abundances in EH and H chondrites of Newsom (1995) [b] bulk silicate Mars estimates from Taylor (2013) and Yang et al. (2015), except for S, Se and Te (Wang and Becker, 2017) and Ge (Righter et al., 2011c) [c] bulk Moon as assumed to be bulk silicate Earth (BSE). Estimates of BSE concentrations are from Wang et al. (2018), except for S, Se, Te, for which we used the estimates of Wang and Becker (2013) [d] Bulk silicate Moon estimates from Hauri et al. (2015). A 20% uncertainty on these estimates was assumed because no uncertainties were reported in the latter study.

4.1.1 The Moon

Steenstra et al. (2017c) showed that the lunar mantle depletions of S, Se, Te can be fully reconciled with their preferential partitioning into the core during differentiation of the Moon, assuming core formation temperatures were close to or at the lunar mantle liquidus at the core-mantle boundary (<2250 K). Subsequent work detailed in Chapter 16 shows that the Ni, Co and Cr systematics of the lunar mantle could reflect much higher temperatures during core formation. The effect of much higher temperatures on volatile element budgets in the lunar mantle should therefore be explored. Our new experimental results can be used to assess whether super-liquidus temperatures during lunar core formation would significantly change our previous conclusions.

Most of the experiments were performed at pressures that are slightly below the pressure at the lunar core-mantle boundary (~5 GPa; Garcia et al., 2011, 2012), and we showed in section 11.3.3 that pressure has a clear effect on the partitioning of S, Se, Te and Cu. The metal-silicate partition coefficients of the latter elements were therefore corrected to 5 GPa, using the pressure dependencies from Steenstra et al. (2017c) for S, Se and Te, which are within error with those found here, and the fit described in Fig. 11.5 for Cu.

Fig. 11.6 shows the required mantle depletions of S, Se and Te (from Steenstra et al., 2017c) and the modeled log $D_{S,\ Se,\ Te}^{met-sil}$ values at 5 GPa as a function of temperature for a lunar Fe-Ni core comprising 1 to 2.5 % of the lunar mass. The depletions of volatile elements S, Se, and Te are fully reconciled with their preferential partitioning into the lunar core at temperatures below ~2800, 2250 and 2500 K, respectively. These results are consistent with our previous findings based on experimental results obtained up to 1883 K (Steenstra et al., 2017c). At higher temperatures (including those required to explain Ni, Co and Cr systematics, see Chapter 16), the negative effects of temperature on log $D_{S,\ Se,\ Te}^{met-sil}$ results in insufficiently siderophile behavior of these elements and additional depletion mechanisms would be required.

Fig. 11.7 shows results of comparable model calculations for Cu, Zn, Ga, Ge, Cd, In, Sn and Pb. An important first observation is that all of these elements, with the exception of Zn, behave siderophile across the whole temperature range considered. In the case of elements Cu, Ge and Sn (Fig. 11.7) their siderophile behavior is sufficient to largely if not fully explain their lunar mantle depletions by preferential partitioning into the lunar core. This is especially true for lower-temperature core formation scenarios. On the other hand, Ga, Cd, In and Pb behave insufficiently siderophile to explain their lunar mantle depletions by core formation only. With increasing higher temperatures of lunar core formation, modeled values of Ga, Cd and Pb approach the required range (Fig. 11.7). Indium and most notably Zn are insufficiently siderophile across the whole range of temperatures considered in this study.

The lunar mantle depletions of P and Sb can be reconciled with lunar core formation, except at temperatures exceeding ~2700 and 2600 K, respectively (Fig. 11.8). At >2700 K, P behaves too siderophile (i.e. P is over-depleted), while Sb abundances following core formation at >2600 K are too low to be reconciled with core formation depletion.

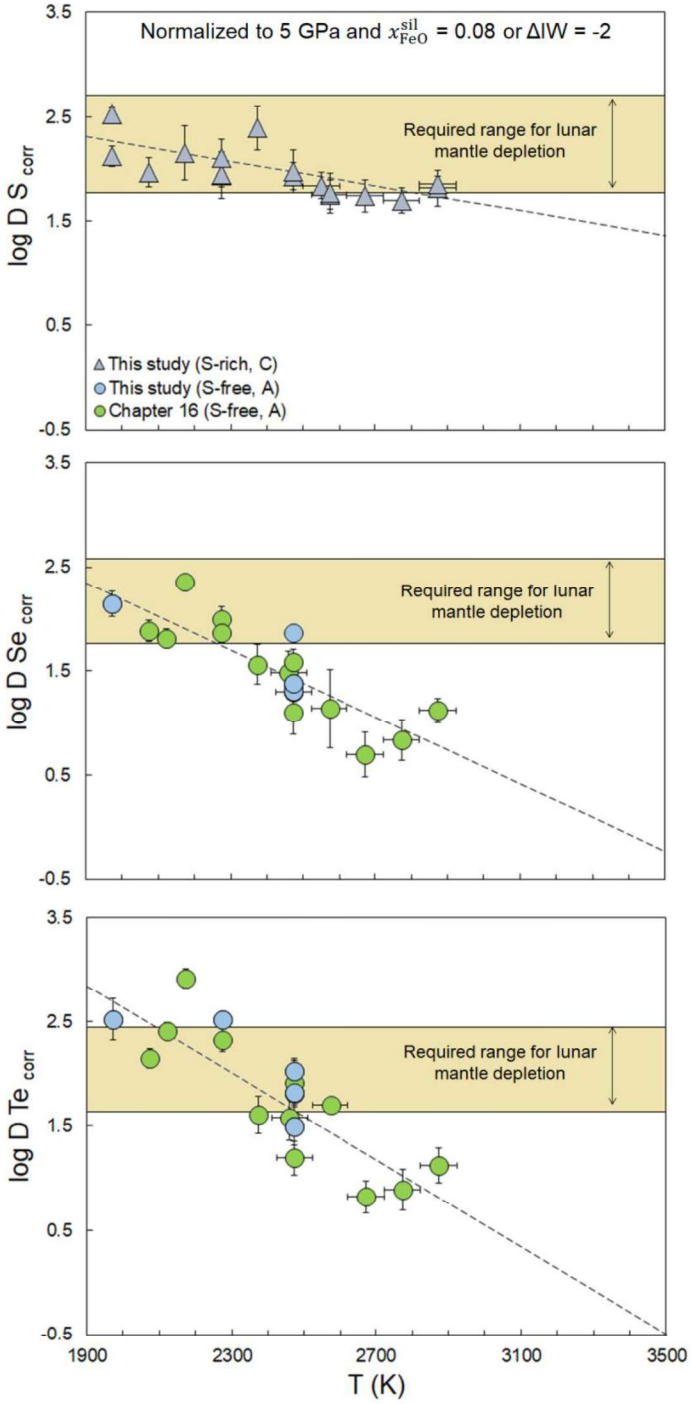

Fig. 11.6 *Metal-silicate partition coefficients of S, Se and Te from this study and Chapter 16, corrected to 5 GPa and $x_{FeO}^{silicate}$ = 0.08 using the relationships reported in Steenstra et al. (2017c), as a function of temperature. Letters denote type of metal mixture used. Horizontal shaded bar represents the required range for explaining the lunar mantle depletions by core formation only and were taken from Steenstra et al. (2017c). Dashed lines represent linear fits to reported metal-silicate partitioning data. Errors represent propagated errors based on 2 SE for EPMA and/or LA-ICP-MS derived concentrations.*

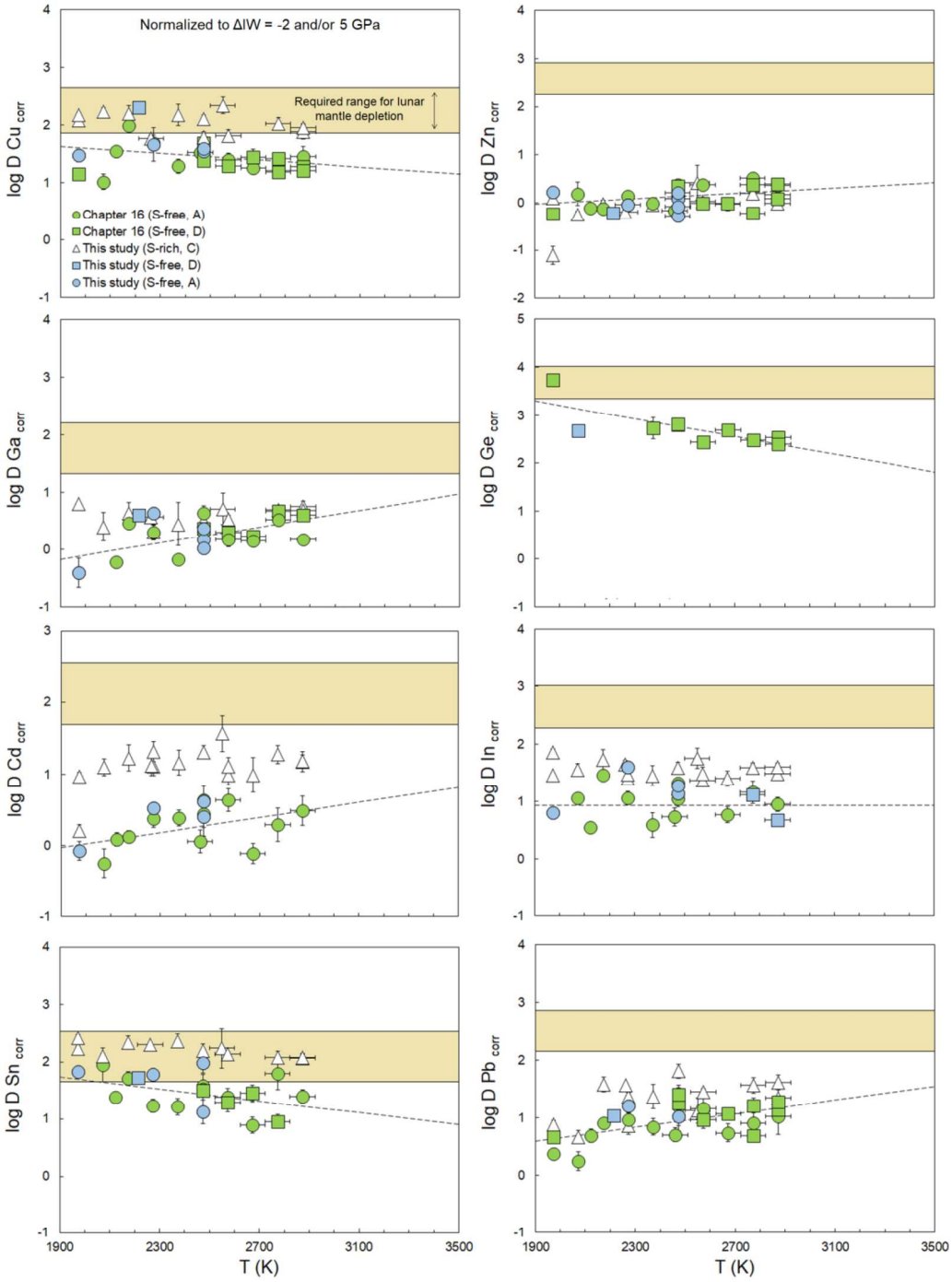

Fig. 11.7 *Metal-silicate partition coefficients of Cu, Zn, Ga, Ge, Cd, In, Sn and Pb from this study and Chapter 16, corrected to ΔIW = –2 assuming a 1+ valence state for Cu, 2+ for Zn, Ge, Cd, Sn, Pb and 3+ for Ga and In. Open triangles represent S-rich experiments (~15 wt.% S). Letters denote type of metal mixture used. Metal-silicate partition coefficients for Cu were normalized to 5 GPa according to the derived pressure dependency (Fig. 11.5). Horizontal shaded bar represents the required range for explaining the lunar mantle depletions (Table 11.4). Dashed lines represent linear fits to reported metal-silicate partitioning data. Errors represent propagated errors based on 2 SE for EPMA and/or LA-ICP-MS derived concentrations.*

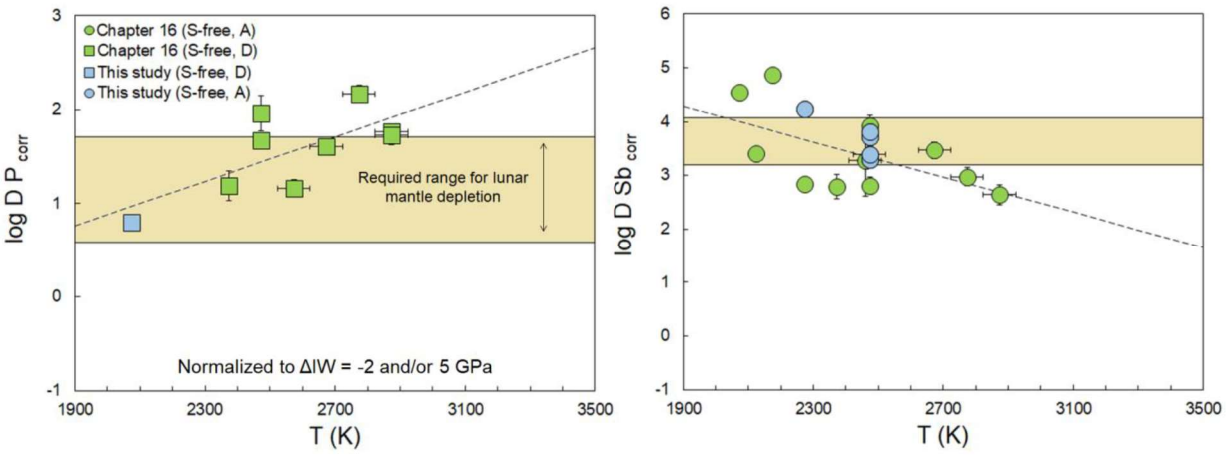

Fig. 11.8 *Metal-silicate partition coefficients of P and Sb, corrected to ΔIW = –2 assuming a 5+ valence state for P and a 3+ valence state for Sb, as a function of temperature. Letters denote type of metal mixture used. Horizontal shaded bar represents the required range for explaining the lunar mantle depletions (Table 11.4). Dashed lines represent linear fits to reported metal-silicate partitioning data. Errors represent propagated errors based on 2 SE for EPMA and/or LA-ICP-MS derived concentrations.*

Although geochemical constraints are generally inconsistent with the existence of a S-rich lunar core (Righter et al., 2017a; Steenstra et al., 2017a; 2018b), it is illustrative to consider the effects of variable S concentrations on the depletion of volatile elements in the lunar mantle. If the lunar core would be S-rich (6–12 wt.% S), as suggested from some geophysical and thermochemical models of the lunar interior (Zhang et al., 2013; Jing et al., 2014; Laneuville et al., 2014; Antonangeli et al., 2015), depletions for most volatile elements would be far more significant. For example, the strongly positive effects of S on Se and Te partitioning would result in an expected increase of ~0.7 log units in log $D_{Se,\ Te}^{met-sil}$ (Steenstra et al., 2017c). The lunar mantle depletions of Cu and Sn can be fully satisfied across the whole temperature range considered if a S-rich core is assumed, whereas addition of S to the lunar core would result in much higher lunar mantle depletions of Ga, Cd, In, and Pb. The effect of S, however, is neglible on the expected depletion of Zn by core formation.

Altogether, these results are largely consistent with previous results of Steenstra et al. (2016a, 2017c), who demonstrated that formation of a lunar core will significantly affect the lunar mantle depletions of volatile elements S, P, Cu, Ga, Ge, Se, Cd, Sn, Sb, Te, Pb. However, an important difference with these models is that their depletions can in most cases not be *solely* reconciled with formation of a lunar core at very high temperatures - especially not in case of a S-poor core in the case for most elements.

4.1.2 Mars

The pressure at the Martian core-mantle boundary is estimated to be ~20 GPa (Rivoldini et al., 2011; Khan et al., 2017). Unfortunately, the effects of pressure on the metal-silicate partitioning of volatile elements at *P* >5 GPa are poorly constrained. As has been shown in previous studies, extrapolation of low-pressure (<5 GPa) trends to high-pressure (>5 GPa) core formation scenarios can result in erroneous results, due to (a) structural transition(s) in Fe-rich alloys that occur at approximately 5 and/or 15 GPa, depending of the type of alloy considered (Morard et al., 2007; Sanloup et al., 2011). At this moment, we can therefore not quantitatively assess whether these elements have significantly partitioned in the Martian core. A qualitative comparison of our new experimental results with the calculated martian mantle depletions show that the relative minor depletions of the various volatile elements, including Cu, Cd, In and Sn, must be strongly affected by formation of a S-bearing Martian core (Fig. 11.9). All depletions are well reproduced by our experimental metal-silicate partition coefficients obtained at ~2550 K and ~4 GPa. Assuming that pressure does not result in significantly lower D values for these elements, core formation appears to be a viable mechanism to explain VSE depletions in the Martian mantle.

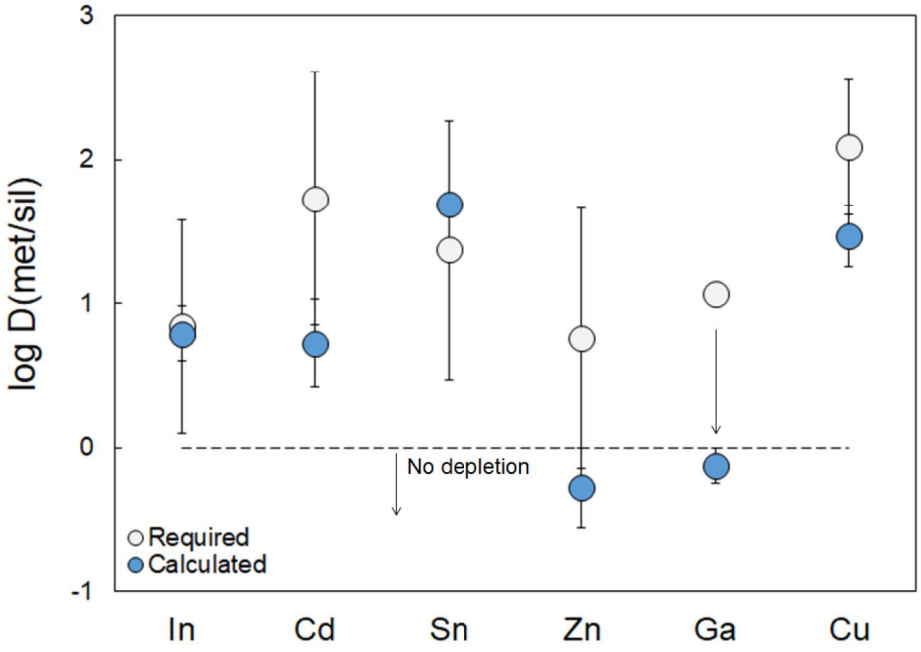

Fig. 11.9 *Comparison between the average of experimentally determined metal-silicate partition coefficients for several VSE from experiments performed with S-rich Fe-alloys at ~2550 K (PR1482, PR1503, PR1549) and calculated D values required for explaining their depletions in the Martian mantle by core formation (Table 11.4). Experimental D values were normalized to ΔIW = –1 (Rai and van Westrenen, 2013) assuming a 1+ valence state for Cu, 2+ for Cd, Sn, Zn and 3+ for In and Ga. Downward arrow for Ga shows the possibly non-depleted nature of Ga in the Martian mantle, relative to proposed bulk Mars compositions (Table 11.4).*

These results are consistent with previous predictions for S, Se and Te (Steenstra and van Westrenen, 2018) and the alkali elements (Steenstra et al., 2018a) as well as with the study of Yang et al. (2015). Any segregation of sulfide phases prior to the formation of the SNC martian meteorite lithologies would also result in strong additional depletions of many volatile elements given their chalcophile behavior (Steenstra et al., 2018b).

11.4.2 Role of volatile loss on VSE abundances in the lunar mantle

Several processes other than core formation can affect the VSE depletions in the lunar mantle, such as their preferential partitioning into sulfides and volatility-related losses during or after the Moon-forming event. As has been demonstrated in previous studies (e.g. Kiseeva and Wood, 2013, 2015; Steenstra et al., 2018b), segregation of sulfides following crystallization of the lunar magma ocean (Morbidelli et al., 2018) and/or during partial melting events in the lunar mantle would significantly deplete the lunar mantle in most volatile elements. Instead, our results are most consistent with interpretations derived from stable isotopic compositions for volatile elements in primitive lunar samples. It is demonstrated in this study that the depletion of S can be fully reconciled with core formation at a wider range of temperatures. These results are consistent with the lack of significant isotopic fractionation of S isotopes between the BSE and the bulk Moon, which implies that less than 10% degassing of S occurred during or after the Moon-forming event (Wing and Farquhar, 2015). The hypothesis that the significant isotopic fractionation of Zn in the bulk silicate Moon, relative to BSE, is due to (a) degassing event(s) during or after formation of the Moon (Paniello et al., 2012), is consistent with the observation that the lunar mantle abundance of Zn is impossible to reconcile with its preferential partitioning into the lunar core, independent of temperature and/or core composition (Fig. 11.7). Although a significant fraction of the bulk Moon Ga budget is expected to partition into the core during core formation, this process alone cannot explain the Ga depletion of the lunar mantle. The additional loss of Ga, besides core formation, agrees with the measured Ga stable isotopic compositions of primitive lunar materials. These results imply that Ga was lost from the Moon following its formation, perhaps during the lunar magma ocean phase (Kato and Moynier, 2017).

11.5 CONCLUSIONS

Both Mars and the Moon likely differentiated at high temperatures. To assess how volatile budgets of the lunar and martian mantle are affected by high temperature core formation processes, high-pressure experiments were performed in which metal-silicate mixtures were equilibrated at high temperatures (1973–2873 K). Our results show that temperature strongly

increases the siderophile behavior of P, Zn, Ga, Cd and Pb and that the siderophile tendency of S, Ge, As, Se, Mo, Sb, Te and Mo is decreased with temperature. Temperature has only a small or negligible effect on the metal-silicate partitioning behavior of Cu, In, Sn and W.

Our results confirm that the depletions of P, S, Se, Te and Sb can be fully reconciled with their preferential partitioning into the lunar core at mantle and core super-liquidus temperatures. Additional depletion mechanisms are required for some of these elements if the Moon differentiated at extremely high temperatures. An important observation is that the lunar mantle abundances of volatile elements Cu, Ga, Ge, In, Cd and Pb are also strongly affected by the formation of a lunar core, but that their overall depletions are unlikely to be fully reconciled with core formation only. Core formation in the Moon also has a neglible effect on mantle Zn abundances. These results are therefore consistent with independent observations of significant isotopic fractionations of Zn and Ga stable isotopic compositions of primitive lunar samples, suggesting that a fraction of these elements was lost during volatility-related processes during the giant impact event and/or during subsequent magma ocean degassing events.

A quantitative assessment of the expected VSE depletions in the Martian mantle is as of yet not possible due to a lack of understanding of the pressure effects on VSE metal-silicate partitioning. However, a qualitative assessment shows that it is likely that core formation in Mars explains a significant fraction of measured VSE depletions in SNC meteorites, due to the S-rich nature of its core and the expected high temperatures during core formation.

Acknowledgements

This work was supported by a Netherlands Organization for Scientific Research (N.W.O.) Vici award to W.v.W. and was partially funded by SFB TRR-170. We would like to thank M. Duncan for her assistance in the experiments presented in this study.